

### 10.3.6.3 Results of Single-Continuum Models

In the single-continuum models, only the fracture-continuum properties of the basalts and the matrix-continuum properties of the surficial sediments and sedimentary interbeds are represented (Table 10.3-3). Shown in Figure 10.3-13 is a comparison of the saturation profile for the single continuum obtained using the computer codes FLOTRAN and FEHM with a numerical solution of Richards equation obtained from Mathematica (Wolfram 1991 [157417]). As can be seen from the figure, excellent agreement is obtained for the two codes, as well as good agreement with the Mathematica solution. The slight offset between FEHM and FLOTRAN can be attributed to differences in the discretization approach used in the codes.

The saturation calculated using the single-continuum model at the end of the 50 yr transient period (2002) is shown in Figure 10.3-14. No significant lateral changes in simulated saturation are present resulting from the higher infiltration rates associated with the waste disposal area in the central part of the model domain. McElroy and Hubbell (1990 [156433], p. 362) reported capillary pressures of 0.2–1.3 bars in the surficial sediments and 0.3–1.3 bars in the 9 m, 34 m, and 73 m interbeds. McElroy and Hubbell (1990 [156433], p. 363) also reported that conditions were wetter at the tops of the sedimentary interbeds than at the bottoms, a condition that is also present across the interbeds in the simulation results (see also Figure 10.3-13).

The relative tracer concentrations (concentration relative to input concentration) at the end of the 50 yr transient period are shown for the upper 80 m of the model domain in Figures 10.3-15a and b for constant and pulse infiltration, the latter representing the flooding events listed in Table 10.3-2. Shown in Figure 10.3-16 is the tracer concentration for both FLOTRAN and FEHM for constant infiltration and pulsed infiltration using FLOTRAN along the centerline of the computation domain. The tracer is applied with unit concentration within the waste-disposal area in the central part of the model domain. Outside this region, a concentration of  $10^{-3}$  is applied. An initial concentration of  $10^{-8}$  is assumed. The model results indicate that a small fraction of a conservative solute could migrate from shallow waste-disposal pits to the 73 m interbed within 50 years, given the infiltration rates and rock properties assumed in this model. The pulse release leads to a somewhat greater penetration depth.

### 10.3.6.4 Results of Dual-Permeability Models

In the dual-permeability models, the basalt fracture-continuum properties and the sediment matrix-continuum properties are the same as in the single-continuum models and, additionally, the basalt matrix-continuum properties and sediment fracture-continuum properties are included. The FLOTRAN code requires that dual-permeability models have a fracture continuum throughout the model domain, but it is unlikely that the unconsolidated sedimentary layers actually contain fractures. Ideally, then, the fracture continuum in the sedimentary layers would be defined in such a way that it transmits negligibly small amounts of water and does not affect the saturations or capillary pressures in the matrix continuum of the same sedimentary layer or in the fracture continuum of the adjacent basalts. Therefore, the fracture-continuum properties and fracture-matrix interaction terms in the sedimentary layers (see note to Table 10.3-3) were chosen to ensure that the water flow rates, saturations, and capillary pressures of the sedimentary layers in the dual-permeability models were nearly identical to the flow rates, saturations, and capillary pressures of the sedimentary layers in the single-continuum models. This was done by

assigning a low volume to the fracture continuum in the sedimentary layers and making the fracture-matrix interaction term large enough to result in the equivalent continuum limit of the dual-continuum model. Hydrodynamic equilibrium between the fracture and matrix continua in the sedimentary layers is maintained and dominated by the properties of the matrix continuum. The approach was verified by comparing the saturation of the matrix continuum in the dual-permeability model with the saturation of the sedimentary layers of the single-continuum model, in a one-dimensional steady-state model with infiltration rate of 1 cm/yr (Figure 10.3-17). Also shown is the numerical solution to Richards equation obtained using the software code Mathematica (Wolfram 1991 [157417]) for the single-continuum case. Saturation of the sedimentary layers in the two models is nearly identical. As expected, saturation of the fracture continuum of the basalt layers in the dual-permeability model is slightly less than that of the basalt layers in the single-continuum model, because a small part of the flux in the dual-permeability model moves through the basalt matrix. In the upper parts of the individual basalt flow units, the fracture continuum and matrix continuum are not in capillary-pressure equilibrium, probably because the large reduction in the fracture-matrix surface area (0.01) limits water flow from the fractures into the matrix. However, capillary-pressure equilibrium is re-established with depth within the flow unit as water flows from the fractures into the matrix.

The simulated saturation profiles for the fracture and matrix continua of the dual-permeability model are shown in Figure 10.3-18 after an elapsed time of 50 years for constant infiltration. Matrix saturations in the basalts are much higher than fracture saturations throughout the model domain because the assumed moisture retention characteristics allow the matrix to retain more water at high capillary pressures than the fractures. The fracture and matrix continua are in approximate capillary-pressure equilibrium above the 73 m interbed, but, similar to the results of the one-dimensional steady-state dual-permeability model (Figure 10.3-17), the matrix capillary pressures just below the 73 m interbed correspond to drier conditions (have higher capillary pressures) than in the adjacent fractures. Gradually, as water flows from the fractures into the matrix, capillary-pressure equilibrium between the two continua is re-established with increasing depth below the 73 m interbed.

The relative tracer concentrations at the end of the 50 yr transient period are shown for the upper 80 m of the fracture and matrix continua in Figure 10.3-19 for the case of constant infiltration. The fracture-continuum relative concentrations (Figure 10.3-19a) are slightly less than the concentrations of the single-continuum model at the same location (Figure 10.3-15a) because some of the tracer has moved into the basalt matrix in the dual-permeability model. The additional storage provided by the basalt matrix prevents the tracer from arriving at the 73 m interbed in the dual-permeability model. However, tracer is present in the 9 m interbed at a relative concentration of 0.06 and in the 34 m interbed at a relative concentration of 0.03, despite the much lower concentrations or absence of the tracer in the overlying basalt matrix (Figure 10.3-19b). Clearly, the tracer distribution in the matrix continuum of the A-B and B-C interbeds reflects the transport of tracer almost exclusively through the fractures of the basalt units.

It should be noted that in the single-continuum models, the basalt layers used the properties listed for the A-, B-, C-, and D-basalts. In the dual-permeability models, these property values were used for the fracture continuum in the appropriate layer, and "basalt matrix" properties were used for the matrix in all basalt layers. All layers (including sedimentary layers) in the dual-permeability model were assumed to have cubic matrix blocks 1 m on a side and a bulk fracture

porosity of 0.01. Fracture-continuum properties of the sedimentary layers were assumed to be the same as those given for the matrix in Table 10.3-2. In the basalt layers, the effective fracture-matrix area calculated from the block dimensions was reduced by a factor of 0.01 based on model calibration results of the large-scale infiltration test (Section 9.3). In the sedimentary layer, the fracture-matrix area was increased by a factor of 100 to ensure hydrodynamic equilibrium between the fracture and matrix continua. The equivalent continuum permeability was twice that given for the interbed matrix permeability.

#### 10.3.6.5 Flow and Transport Simulations with Dipping, Discontinuous Layers

The previous simulations in Sections 10.3.6.3 and 10.3.6.4 have considered an idealized hydrostratigraphy for the SDA in which layers are horizontal and of uniform thickness. In contrast, structural contour and isopach maps (see Section 10.3.3) indicate that the SDA is located in an area where the surficial-sediment/basalt interface is relatively low and where the interbeds have variable thicknesses and dips. To examine the effect that departures from the idealized stratigraphy of the previous case might have on flow and transport beneath the SDA, investigators created a model with the computer code FEHM that considers the structural depression in the A-basalt beneath the SDA and treats the 9 m and 34 m interbeds as dipping discontinuous layers (Figure 10.3-20). The C-D interbed is horizontal with uniform thickness, as in the previous calculations.

The FEHM model is based on a single-continuum representation with the same hydrologic properties as used in the previous single-continuum models (Table 10.3-3). The FEHM model has a constant vertical node spacing of 0.5 m and horizontal node spacing of 1.0 m. In this model, the pulses of water associated with flooding events are not used; instead, the flux in the central 12 m of the model domain was increased to 10 cm/yr during the 50 yr transient period to implicitly account for these events. This led to slightly more water being introduced into the UZ than in the previous models for the last 50 yrs (5 m for this model compared with the 4.61 m of water introduced for the cases with flood events).

For a steady-state uniform infiltration rate of 1 cm/yr, flow-lines calculated by particle tracking in FEHM indicate that the clay layer at the base of the surficial sediment strongly focuses flow toward low areas in this layer beneath the hypothetical SDA, at the center of the model domain (Figure 10.3-21). The interbeds also divert water laterally along their upper surface, but the amount of offset for the flow lines is less than 5 m at any interbed. Because water flow is focused by the slope of these layers, wetter conditions exist at low points in the clay layers and where the interbeds terminate, even when infiltration rates are uniform. (Note that water potentials were calculated by subtracting a uniform air pressure of 1 bar from the calculated water pressure; a water potential of 0 bars indicates saturated conditions.)

Saturations calculated at the end of the 50 yr transient period, in which 10 cm/yr of infiltration was applied in the central 12 m of the flow domain, indicate that the basalts are wettest below the ends of the overlying interbeds (Figure 10.3-22). Tracer concentrations near the water table at the end of the 50 yr transient period are highest where the 34 m interbed has focused water flow (Figure 10.3-3). Peak tracer concentrations at the water table are about 0.12 compared to peak concentrations of about 0.05 for the case with uniform, horizontal layers. Although slightly more water was applied in the case with discontinuous layers, the pattern of saturation (Figure 10.3-

22) and tracer concentrations (Figure 10.3-23) suggests that part of the early breakthrough is caused by some water flowing around rather than through the high-porosity interbeds. Also, flow rates are relatively high where flow is focused by the dipping, discontinuous layers.

### 10.3.6.6 Reactive Transport Calculations

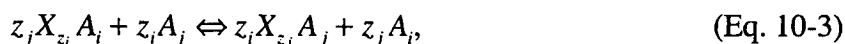
In this section, vertical radionuclide transport through the surficial sediment zone in the SDA is investigated. Using representative soil-zone water and  $P_{CO_2}$ , along with surface site density, cation exchange capacity, and mineralogy of the soil zone, sorption profiles for  $^{241}Am$ ,  $^{238}Pu$ ,  $^{137}Cs$ , and  $^{90}Sr$  were calculated and compared with field observations. The resulting model calibration predicts a high retardation factor for Np and essentially no retardation for U.

#### 10.3.6.6.1 Sorption Reactions: Surface Complexation and Ion Exchange

Both surface complexation reactions and ion exchange are included in the description of sorption. The radionuclides americium and plutonium take part in surface complexation reactions, and cesium takes part in ion exchange. Strontium is involved in both sorption processes. The generic form of surface complexation reactions can be written as



where  $X_m^\alpha$  denotes the surface site of type  $\alpha$ ,  $A_j$  an aqueous primary species,  $A_k^{m\alpha}$  the sorbed surface complex, and  $\nu_{jk}^{m\alpha}$  the stoichiometric coefficient matrix. This description neglects the role played by the counter ion and therefore does not conserve charge separately within the aqueous and solid phases whenever the surface complex is charged. It is presently unknown what effect this inconsistency may have on predicting retardation and changes in solution chemistry, such as pH (Lichtner 1996 [101409], pp. 57–59). Ion exchange reactions have the form



where  $X_{z_i} A_i$  refers to the sorbed cation. These reactions conserve charge rigorously in both aqueous and solid phases, unlike the representation used for surface complexation reactions. Sorption reactions for surface complexation included in the model calculations are listed in Table 10.3-4 along with corresponding selectivity coefficients. The data were taken from Zavarin and Bruton (2000 [156443] and 2000 [156444]). Cations taking part in ion exchange reactions are listed in Table 10.3-5, along with their selectivity coefficients. The data were adapted from generic values given in Appelo (1996 [156425]).

Generally, sorption reactions involve multiple sorption sites associated with different mineral surfaces. Two distinct philosophies have been articulated in the literature (Davis et al. 1998 [154436]) for modeling sorption reactions. One approach is to develop a detailed model based on the specific minerals present in the sorbing medium. This approach has the advantage of being more mechanistically based and having the potential capability of incorporating changes in mineral abundances on sorption. Its primary disadvantage is the extensive amount of data required as input parameters to the sorption model. An alternative approach is based on the bulk properties of the porous medium. This approach is more phenomenological, but has fewer data

requirements. It is based on direct measurements of bulk properties such as cation exchange capacity (CEC) and surface site densities. In this report, the bulk approach is used, employing a multisite description of surface complexation reactions and a single-site representation of ion exchange reactions.

For a dilute aqueous solution, retardation of a particular primary species is derived from the distribution coefficient  $K_j^D$ , defined as the ratio of total sorbed to total aqueous concentration of that species

$$R_j = 1 + K_j^D \quad (\text{Eq. 10-4})$$

The distribution coefficient is given by the expression

$$K_j^D = \frac{1}{\phi \Psi_j} \left[ \sum_{k\alpha} v_{jk}^{m\alpha} \Xi_k^{m\alpha} + \Xi_j^{ex} \right] \quad (\text{Eq. 10-5})$$

involving a sum over surface complexation and ion exchange isotherms, where  $\Xi_k^{m\alpha}$  refers to the sorbed concentration of surface complex  $A_k^{m\alpha}$ , and  $\Xi_j^{ex}$  refers to the ion exchange isotherm. The quantity  $\Psi_j$  represents the total aqueous concentration of the subscripted species.

Sorption reactions used for surface complexation include the surface sites:  $>\text{FeOH}$ ,  $>\text{SiOH}$ ,  $>\text{AlOH}$ , and  $>\text{Ca}^{2+}$ . Unknown is the appropriate site density to use in the calculations. The site concentration associated with the  $m$ th mineral, denoted by  $n_\alpha^m$  [mol/dm<sup>3</sup>], can be expressed as a product of a number of factors involving the intrinsic mineral site density ( $\eta_\alpha^m$  [# sites/nm<sup>2</sup>]), mineral concentration ( $\rho_m \phi_m$  [kg/dm<sup>3</sup>]), and mineral specific surface area ( $A_m$  [m<sup>2</sup>/kg]). Thus, the site concentration can be calculated from

$$n_\alpha^m = \frac{1}{N_A} \eta_\alpha^m A_m \rho_m \phi_m \quad (\text{Eq. 10-6})$$

where  $N_A$  denotes Avogadro's number, the intrinsic site density is denoted by  $\eta_\alpha^m$ , and the specific surface area is represented by  $A_m$ .

Retardation caused by ion exchange is proportional to the CEC of the exchanging medium and the bulk rock density. The conventional definition of the CEC is in units of meq/100 g solid. A more useful quantity is mole equivalents of exchange sites per bulk volume of porous medium, denoted by the symbol  $\omega$ . The two quantities are related by the porosity and grain density of the porous medium

$$\omega = (1 - \phi) \rho_s \text{CEC} \quad (\text{Eq. 10-7})$$

where  $\rho_s$  denotes the grain density and  $\phi$  the porosity. Retardation is proportional to  $\omega$  and, thus, to the product of the bulk density and the CEC.

### 10.3.6.6.2 Model Simulations

Calculations were performed in one dimension with a constant infiltration Darcy flow rate of 10 cm/yr, a porosity of 50%, and an average saturation of 0.58 (Magnuson and Sondrup 1998 [156431], p. 4-8, Table 4-2). Radioactive decay was not included in the simulations. An aqueous diffusion coefficient of  $10^{-5}$  cm<sup>2</sup>/s with a tortuosity of 0.294 taken from Magnuson and Sondrup (1998 [156431], Table 4-2, p. 4-8) for the surficial sediment layer was used in the simulations.

The injection fluid composition is listed in Table 10.3-6. The fluid composition is taken from Well 99 corresponding to perched water as listed in Table 10.3-1. The pH was adjusted to give equilibrium with calcite, which otherwise would have been supersaturated by one log unit. This adjustment resulted in a reduction in the reported pH of 8.4 to 7.59. The redox state of the fluid is not given in Table 10.3-1. As discussed below, to obtain a simultaneous fit to the concentration profiles for plutonium and americium, it was necessary to invoke reducing conditions. The initial fluid composition was set to be the same as the injection fluid, with the exception of the radionuclide concentrations: plutonium, americium, cesium, uranium, and neptunium, which were set to small values ( $10^{-20}$  mol/L) and strontium, which was given the value of  $5 \times 10^{-16}$  mol/L to fit the minimum observed strontium value. It was not determined how much of the strontium profile resulted from nonradioactive strontium that was naturally occurring. The calculated  $\log P_{\text{CO}_2} = -2.18$ , which is quite high, presumably resulted from decomposition of organic matter in the waste and soil zones. As can be seen by inspection of Table 10.3-6, carbonate complexes play an important role in speciation of americium and uranium and less so for neptunium. Plutonium exists primarily in the IV oxidation state in the form of the complex  $\text{Pu}(\text{OH})_4$ .

The observed sorbed concentration profiles were fit by adjusting the surface site densities and the injected radionuclide concentrations. Site densities  $>\text{FeOH}$ ,  $>\text{AlOH}$ , and  $>\text{SiOH}$  were adjusted to fit the observed profiles. The  $>\text{Ca}^{2+}$  site density was arbitrarily set to  $10^{-4}$  mol/L. The resulting site densities used in the simulations are listed in Table 10.3-7.

Speciation results of the injection fluid for the amount sorbed for different radionuclides participating in surface complexation are presented in Table 10.3-8, in which the contribution to the distribution coefficient is listed for each surface site. It can be seen that plutonium contains contributions from sorption sites  $>\text{FeOH}$  and  $>\text{AlOH}$ , whereas americium is primarily sensitive to site  $>\text{AlOH}$  and to a lesser extent site  $>\text{Ca}$ . There were no data available for uranium and neptunium. The distribution coefficients are much smaller than those reported by Dicke (1997 [157410]) as listed in Table 9.3-1.

An entirely different result is obtained under oxidizing conditions. In this case, both plutonium and americium are strongly sorbed to  $>\text{FeOH}$ , with americium several orders of magnitude greater compared to plutonium. Because under oxidizing conditions plutonium is not sorbed to any other sites, it is not possible to fit the plutonium and americium profiles simultaneously under these conditions.

Generic values for the ion exchange selectivity coefficients (see Table 10.3-5) were taken from Appelo (1996 [156425]). The CEC was varied to fit the cesium profile. A value of 0.02 mol/kg was obtained. This value is at the lower limit of the reported CEC range for the surficial

sediments of 0.27 to 0.02 mol/kg (Rightmire and Lewis 1987 [156441], Table 5). The strontium profile was predicted by the model without any additional fitting.

The resulting fit to the data is shown in Figure 10.3-24, corresponding to advection and diffusion. The obtained fit does not capture the observed decrease in plutonium concentration at depth of approximately 1 m. This discrepancy could be a result of several factors, including heterogeneity, lateral flow, and the possibility of the presence of the contact between the clay and basalt layer that occurs at this depth. Other species also indicate a slight increase in concentration at this depth.

### 10.3.7 Discussion

Several interpretations of radionuclide transport in the surficial sediment zone are possible. One is that lateral flow occurred, sweeping out part of the radionuclide plume. The thickness of the stratigraphic layers is highly irregular, and the possibility exists that flow occurred along the interface between the clay layer and the surficial sediment layer. Another possibility is that a catastrophic or sudden release of a pulse of fluid, caused by a flooding event, released a pulse of radionuclides that propagated downward with reduced retardation, due to kinetic effects caused by fast flow rates. For this situation, the data are interpreted as background flow (or diffusion) producing the upper monotonically decreasing profile with depth. The lower portion of the profile, where the concentration is increasing was the result of a sudden flow event. Presumably, according to this interpretation, the peak lies at a still greater depth below that at which the data were collected.

The model calculations predict retardation factors for neptunium and uranium that are seen to be orders of magnitude higher compared to the other radionuclides. This result would indicate that very little movement of neptunium and uranium should be observed. No values for these radionuclides were reported that could be taken as consistent with their predicted high retardation.

Finally, although it was necessary to assume reducing conditions for fluid coming from the SDA, it is not expected that such conditions would persist at greater depths because of the partially saturated conditions that are present there, leading to oxidizing water.

### 10.3.8 Conclusion

The main conclusion to be drawn from this study is that INEEL presents a far wetter environment than that of Yucca Mountain. This increase in infiltration is manifested in higher infiltration at the SDA and flooding events that could have resulted in enhanced radionuclide migration beneath the SDA. Focused flow resulting from the undulating topography of the basalt flows and sedimentary interbeds would be expected to exacerbate the situation, leading to even greater distances of radionuclide migration, as demonstrated in the modeling exercises.

It was found that to fit observed radionuclide concentrations in the surficial sediment layer, reducing conditions were required. Otherwise, it was not possible to fit the observed profiles of both americium and plutonium simultaneously. Note that although detailed waste compositions are not currently known, there is significant organic matter in the waste that is not inconsistent with the assumption of reducing conditions. However, as noted above, such conditions are not

expected to prevail at greater depths, where the system would be expected to be oxidizing. The calculated profiles did not capture the increase in concentration observed at greater depth near the base of the surficial sediment layer. To further test and validate model predictions, continuity of data at greater depths beneath the SDA would be needed along with site-specific data for surface complexation site densities.

## **10.4 RADIONUCLIDE FLOW AND TRANSPORT STUDIES AT PEÑA BLANCA, MEXICO**

### **10.4.1 Objectives**

The goal of these studies is to construct a three-dimensional conceptual model of the transport of uranium and radiogenic daughter products at Peña Blanca, Mexico (*Technical Work Plan for Natural Analogue Studies for License Application* (BSC 2001 [157535], p. 4)). A three-dimensional model will extend the previous work at Peña Blanca that was limited to collection of data for exposed planar surfaces. The model will also address whether there has been preferential flow/drainage downward through fractures or if there has been a net flux of uranium off-site. To accomplish this, three wells will be drilled at the site to obtain core samples from within and beneath the uranium ore body and to collect water samples from beneath the ore body. The core and water samples will be analyzed using a variety of techniques to support development of the conceptual model of transport at Peña Blanca. The conceptual model will then be tested using numerical methods employed by the UZ Flow and Transport Model to build confidence in understanding UZ transport at a potential Yucca Mountain repository.

### **10.4.2 Background**

In the 1970s, the Peña Blanca region, approximately 50 km north of Chihuahua City, was a major target of uranium exploration and mining by the Mexican government. Since that time the Nopal I uranium deposit has been studied extensively because it is a good analogue for evaluating the fate of spent fuel, associated actinides, and fission products at a geologic repository in unsaturated volcanic tuff. Previous studies associated with Peña Blanca as well as a geologic description of the site were reviewed in *Natural Analogs for the Unsaturated Zone* (CRWMS M&O 2000 [141407]). Briefly, the Nopal I uranium deposit at Peña Blanca represents an environment that closely approximates that of the potential high-level radioactive waste repository at Yucca Mountain, Nevada, in the following ways:

- Climatologically: both are located in semi-arid to arid regions
- Structurally: both are parts of a basin-and-range horst structure composed of Tertiary rhyolitic tuffs overlying carbonate rocks
- Hydrologically: both are located in a chemically oxidizing, UZ 100 m or more above the water table
- Chemically: the alteration of uraninite to secondary uranium minerals at Nopal I may be similar to the eventual fate of uranium fuel rods in a potential geologic repository like Yucca Mountain.



### 10.4.3 Previous Radionuclide Transport Studies at Peña Blanca

Studies of uranium-series disequilibria within and around uranium deposits can provide valuable information on the timing of actinide mobility and hence the undisturbed stability of a potential repository over the geologic time scales associated with the required lifetime of the facility. Previous studies at Peña Blanca dealing with bulk samples and fractures have focused on the extent and timing of uranium-series mobility or transport at this site, and have been summarized in *Natural Analogs for the Unsaturated Zone* (CRWMS M&O 2000 [141407]). Some of these studies reported open-system behavior, suggesting mobility of uranium and its daughter products. In contrast, previous uranium-series thermal ionization mass spectrometry (TIMS) work at Nopal I (CRWMS M&O 2000 [141407], pp. 89–90) found closed-system behavior, suggesting very limited mobility in fracture-filling material for uranium. Briefly, the TIMS results indicated that the uranium (235, 238), thorium, and protactinium in the fracture-filling minerals have remained stable for more than 300 ka at Nopal I.

Pickett and Murphy (1999 [110009]) presented measurements of U-Th isotopic composition and concentration in various water samples collected near the Nopal I uranium deposit during relatively wet conditions (see 1995 collections in Table 10.4-1). The observed uranium and thorium concentrations generally correlate with concentrations of major cations and anions and total conductivity, which may reflect evaporation-dilution or rock dissolution effects on all of these species. Thorium and uranium concentrations also correlate strongly with each other, which is surprising given the expected differences in solution chemistry and potential solubility controls for these two elements. Pickett and Murphy (1999 [110009], p. 812) interpreted these concentrations in the context of solubility control by various uranium silicate minerals (haiweeite, soddyite) and thorianite. They found that the perched water is close to solubility for haiweeite, a calcium uranyl silicate mineral. All of the other waters are undersaturated with respect to uranium mineral phases. However, all of the waters are supersaturated with respect to thorianite, which is attributed to the presence of colloidal thorium in the  $<0.2 \mu\text{m}$  fraction of these samples. The occurrence of undersaturation for uranium and supersaturation for thorium indicates that radionuclide transport in the UZ may be controlled by kinetic factors such as evaporation, rock dissolution, and colloid formation, which complicate the interpretations based on thermodynamic (solubility) considerations. The incorporation of kinetic factors will be discussed below with respect to the generalized radioisotope transport model of Ku et al. (1992 [109939]).

### 10.4.4 Ongoing Work at Nopal I

As previously summarized, prior work at Peña Blanca contrasts the long-term stability of uranium and thorium in fractures against the ongoing dissolution of uranium by surface waters, as evidenced by elevated uranium concentrations and  $^{234}\text{U}/^{238}\text{U}$  in adit seepage waters. The net flux off-site is not well constrained other than by the  $8 \pm 5$  m.y. age of the primary uranium mineralization at Nopal I (Pearcy et al. 1994 [100486], p. 729). Current (2002) work is discussed in the following subsections.

#### 10.4.4.1 Drilling

The goal of current work (BSC 2001 [157535], p. 4) is to extend geochemical studies to the third dimension by drilling wells at Nopal I. Work is now underway to drill one borehole through the uranium ore deposit to a depth of approximately 200 m. The borehole is planned to penetrate the SZ to at least 20 m, and core will be collected during drilling. In addition, two additional wells will be drilled at approximately +50 m and -50 m from the borehole. Monitoring wells will be installed to sample ground water on a quarterly basis.

#### 10.4.4.2 Surface Water Sampling

The work of Pickett and Murphy (1999 [110009]) has been extended to include water samples collected at Nopal I during the dry season. Samples were collected in February 2000 and March 2001 (Simmons 2002 [157544], pp. 86–87). These data provide new information on temporal and seasonal variations at the site (see Section 10.4.4.4). As with the previous work, samples are of three different types: (1) perched water trapped in an old borehole about 20 m outside the deposit, (2) seep water obtained from an old adit approximately 8 m below the +10 m surface (see Figure 10.4-1), and (3) a groundwater sample located in the regional carbonate aquifer 1.3 km southeast of the deposit. In addition, data has been collected from an old mining camp well located about 0.6 km southeast of the deposit.

These new data, along with the 1995 data from Pickett and Murphy (1999 [110009]), are detailed in Table 10.4-1. In many cases, the new data show higher uranium concentrations ratios than the results from Pickett and Murphy for samples collected during the wet season. This could result from longer fluid/rock interaction times or from greater evaporation. A portion of the collection system is shown in Figure 10.4-2. The water is collected in plastic sheets, in which it remains until sampled. Although the adit is comparatively cool and damp, evaporation could greatly influence the uranium concentrations.

Stable isotope data were obtained for some of these adit samples to evaluate the effects of evaporation on the uranium concentrations. These data are shown in Figure 10.4-3. When water evaporates, the isotopic composition of the resulting vapor will be shifted to lower values of  $\delta^{18}\text{O}$ , and the residual water will be shifted to higher values on a plot of  $\delta\text{D}$  versus  $\delta^{18}\text{O}$ . The stable isotope data for AS-5 (from a water well) and AS-6 (from a drill hole into a perched water horizon) have significantly lower values than other samples. They fall on the Global Meteoric Water Line (GMWL) and probably represent the average composition for the precipitation at the site. The adit samples all lie much higher on this plot. Of these, AS-2, AS-3, and AS-4 all fall significantly to the left of the GWML and may represent atmospheric water vapor that has diffused into the adit and condensed in the cooler, underground environment, followed by some period of evaporation in the collection system. AS-1 lies on the GMWL, but probably does not represent a rainwater sample, because it is relatively high for meteoric water at this latitude; it is closer to the opening of the adit and may represent a more evaporated version of cluster AS-2, AS-3, and AS-4. The evolution of stable isotopes for the adit samples appears to have at least three components: (1) evolution of vapor from GMWL, (2) modification by water/rock interaction, and (3) evaporation in the adit collection system. A simpler approach planned for evaluation is to normalize the uranium data to chloride or bromide concentrations.

#### 10.4.4.3 Radioisotope Transport Modeling

A model based on naturally occurring uranium- and thorium-series disequilibria is being tested for characterization of the *in situ* migration of actinide nuclides in and around the Nopal I uranium deposit. Estimates can then be made of the rates of sorption-desorption, hence retardation factors, and dissolution-precipitation of the isotopes over a range of time scales, in both the SZ and UZ. Such information is vital to testing or validating performance assessment models for geologic nuclear waste disposal.

Current models utilizing uranium- and thorium-series disequilibria for radioisotope transport in geologic systems are primarily based on the steady-state flow assumption (Ku et al. 1992 [109939], pp. 639,640). These models, while elucidating the behavior of radioisotopes in the phreatic zone, may not sufficiently constrain the isotope transport in unsaturated vadose layers where the concentration and transport behavior of radioisotopes are often governed by nonsteady conditions. During the past year, the uranium-series transport model of Ku et al. (1992 [109939]) has been extended to include the nonsteady-state situations. Free of the steady-state assumption, this new, generalized radioisotope transport model has the two important features of being applicable to both the SZ and UZ, and providing simultaneous constraints on the behavior of radioisotopes in dissolved, colloidal, sorbed, and solid pools of a groundwater system.

The model makes the following assumptions: (1) in natural water-rock systems, radionuclides reside in four "pools"—dissolved, colloidal, sorbed, and solid—with the colloidal pool being treated as a mobile particle pool; (2) radionuclides in the sorbed and colloidal pools are in first-order sorption equilibrium with those in the dissolved pool; (3) radionuclides in the solid pool are transferred to the dissolved pool through dissolution and  $\alpha$ -recoil, whereas those in the dissolved pool are incorporated into the solid pool through precipitation.

The data in Table 10.4-1 have been analyzed using this model. In contrast to the thermodynamic modeling of Pickett and Murphy (1999 [110009]), this model provides a means to characterize kinetically controlled radionuclide transport at Peña Blanca. The uranium data from the 1995 wet-period measurements are shown in Figure 10.4-4.

As predicted by the model, a linear relationship exists between  $^{234}\text{U}/^{238}\text{U}$  and  $1/^{238}\text{U}$  in waters collected from the vadose zone near the Nopal I uranium deposit (Figure 10.4-4a), due to  $\alpha$ -recoil-induced  $^{234}\text{U}$  enrichment in the water. The one sample from the carbonate aquifer (SZ) shows a much lower  $^{234}\text{U}/^{238}\text{U}$  ratio, perhaps caused by prolonged interaction with old calcites in the aquifer, allowing uranium exchange between rock and solution to mask the effect of  $^{234}\text{U}$  enrichment in the water. Using the model as well as the slope and intercept from Figure 10.4-4a, the relative input rates of uranium from solids to the solution through dissolution and  $\alpha$ -recoil can be derived. The  $^{234}\text{U}$   $\alpha$ -recoil rate for the adit fluids is calculated to be  $\sim 9$  dpm/L/yr. The dissolution rates are  $\sim 8.3$  dpm/L/yr for  $^{238}\text{U}$  and  $^{234}\text{U}$  (or  $47 \times 10^{-9}$  mol/L/yr for  $^{238}\text{U}$  and  $2.6 \times 10^{-12}$  mol/L/yr for  $^{234}\text{U}$ ).

The model also allows determination of the fluid transit time ( $\tau_w$ ) in the UZ. Because of the short transit time of water in the UZ,  $^{238}\text{U}$  concentrations increase linearly with increasing  $\tau_w$  (Fig. 10.4-4b). Meanwhile, the  $^{234}\text{U}/^{238}\text{U}$  ratio decreases rapidly with increasing  $\tau_w$  and very high  $^{234}\text{U}/^{238}\text{U}$  ratios can occur when the water has a very short transit time in the UZ. It is estimated

that the transit time for the seep water that infiltrated into the Level +00 adit 8 m below the surface is about 6–29 days; for the perched water at 10.7 m depth in an old borehole, the transit time is about 0.4–0.5 years. The large values of  $\tau_w$  for the perched water may reflect the long residence time of water in the borehole. Note that because water at different sites may have different pathways, the value of  $\tau_w$  itself does not provide information on possible connections between the perched and seep waters sampled. In conclusion, although the water transit time in the UZ is quite short, significant dissolution of uranium may have occurred in a low-water flux, high-uranium concentration setting near the Nopal I uranium deposit.

#### 10.4.4.4 Seasonal Variability of Uranium Dissolution Rate in UZ

To assess temporal variations in the transport of uranium in the UZ, samples of perched and adit seep waters were collected during the dry winter season in late February 2000 and again in early March 2001. The results are plotted in Figure 10.4-5a. Compared with samples collected during the September wet season of 1995, many of these new measurements show much higher  $^{238}\text{U}$  concentration and lower  $^{234}\text{U}/^{238}\text{U}$ , suggesting increased uranium dissolution and/or lower  $\alpha$ -recoil associated  $^{234}\text{U}$  enrichment rates during the dry season. The low humidity during the dry season may have also enhanced evaporation, causing higher uranium concentrations in the waters sampled.

The data collected during the winter dry season depart considerably from the linear relationship between  $^{234}\text{U}/^{238}\text{U}$  and  $1/^{238}\text{U}$  predicted by the model for the wet season of 1995 (Figure 10.4-5a). Such a departure could result from: (1) high and variable evaporation under low humidity conditions and (2) incomplete flushing associated with low rainfall during the dry season. Linear regressions on data for the perched and adit seep waters collected during March 2001 give a  $^{234}\text{U}$   $\alpha$ -recoil rate ( $\lambda P_r$ ) of  $\sim 5.7$  dpm/L/yr. Compared to the  $\sim 9$  dpm/L/yr for the wet season, this lower  $\alpha$ -recoil rate estimate may reflect incomplete flushing of waters through the vadose layers during the dry season. Dissolution rates of uranium are estimated to be about 24 dpm/L/yr for  $^{238}\text{U}$  and  $^{234}\text{U}$  (or  $136 \times 10^{-9}$  mol/L/yr for  $^{238}\text{U}$  and  $7.5 \times 10^{-12}$  mol/L/yr for  $^{234}\text{U}$ ). These rates are about three times higher than those in the wet season, possibly suggesting a favorable physiochemical condition (e.g., increased oxygenation) for uranium dissolution during dry periods. In this context, it should be noted that the samples collected 15 m from the adit entrance show  $^{234}\text{U}/^{238}\text{U}$  values lower than secular equilibrium, which suggests dissolution of material previously preferentially depleted in  $^{234}\text{U}$  by  $\alpha$ -recoil effects.

Note in addition that large variations in the  $^{238}\text{U}$  concentration and  $^{234}\text{U}/^{238}\text{U}$  ratio were also found in samples collected from the SZ during the dry season (Figure 10.4-5b). While no clear correlation between  $^{238}\text{U}$  and  $^{234}\text{U}/^{238}\text{U}$  is seen, the plots suggest that both the decreased water infiltration flux and the increased uranium dissolution rates in the vadose zone may contribute to the higher dry-season uranium concentrations in the SZ. Observations such as these may have important implications for the effects of climate change on the long-term stability of uranium in the environment.

#### 10.4.5 Work in FY02

Although the data and modeling discussed above provide useful preliminary data for uranium transport at Peña Blanca, spatial dependence and the net flux of uranium transport from the

deposit via groundwater cannot be thoroughly evaluated without higher resolution sampling of any potential groundwater uranium plume in the vicinity of the deposit. This will be accomplished through the drilling program at Nopal I (BSC 2001 [157535], pp. 4–5).

In addition to the core and fluid samples from the borehole and wells, the perched, seep, and aquifer waters from the sites previously sampled will be resampled (see above). Where adequate samples can be obtained, isotopes will be measured of uranium ( $^{234}\text{U}$  and  $^{238}\text{U}$ ), thorium ( $^{232}\text{Th}$ ,  $^{230}\text{Th}$ ,  $^{228}\text{Th}$ , and  $^{234}\text{Th}$ ), radium ( $^{226}\text{Ra}$ ,  $^{228}\text{Ra}$ ), polonium ( $^{210}\text{Po}$ ) and lead ( $^{210}\text{Pb}$ ) in the fluid samples. Radioactive disequilibria in sorbed phases will also be studied, using leaching methods on the core samples. Since it may be difficult to collect enough fluids from the UZ for all of the proposed measurements, data on the sorbed phases should provide an alternative way to assess the radionuclide transport in the UZ.

The U-series modeling effort will be extended to the thorium and radium isotopes. Measurements of polonium and lead isotopes will be applied to the Th model to further evaluate the role of colloids in the transport of these nuclides. Modeled results on uranium transport may be affected by the evaporative concentration in UZ fluids. To correct for this possible effect, the chloride or stable isotope measurements made on water samples from the UZ will be compared with those on rainwater. Model sensitivity and validity will be tested, and ways to evaluate the uncertainties of model parameters will be sought. Results from the Peña Blanca analogue study will be provided for testing the UZ process model.

## 10.5 OTHER TRANSPORT ANALOGUES

### 10.5.1 Steenkampskraal

The Steenkampskraal monazite mine, located about 100 km south of Vaalputs, South Africa, provides an example of colloidal transport of radionuclides in the UZ (Figure 10.5-1). Steenkampskraal is a licensed low-level waste radioactive-waste disposal site in South Africa that is being considered as a potential high-level waste disposal site. Steenkampskraal is the richest monazite ore body in the world. From 1952 to 1963 it was the world's leading producer of thorium and rare earth elements (REE), with total production estimated at 50,000 metric tons of monazite concentrate, containing 45 wt % REE oxides, 4% thorium oxide, and 600 ppm uranium oxide (Jarvis et al. 1997 [157489], p. 12). Monazite and fluorapatite together constitute approximately 80% of the ore mass, along with minor sulfides, oxides, and silicates. Locally, the ore shows enrichment of Fe/Ti oxides. The mine is situated within the granulite facies high-temperature zone of the Namaqualand Metamorphic Complex, where model U-Pb ages of the mineralization are given as  $1180 \pm 40$  Ma (Jarvis et al 1997 [157489], p. 12).

A characterization study was undertaken to investigate the degradation of monazite and apatite and to assess the extent of uranium, thorium, and REE transport away from the primary ore body under *in situ* conditions. One of the main objectives of the study was to evaluate the role of colloids in promoting the mobilization and retardation of trace metals. The average rainfall in the area is 70 mm/yr (Jarvis et al. 1997 [157489], p. 15). Upper sections of the mine experience permanently unsaturated conditions. The steady-state level of the water table is 50 m below the surface when pumping is stopped. The pH of the waters ranges from 7.3 to 8.4 (Jarvis et al. 1997

[157489], p. 21). Analyses of waters collected from boreholes indicate supersaturation by 2 to 3 orders of magnitude with respect to amorphous uranium ( $\text{UO}_2$ ) and thorium ( $\text{ThO}_2$ ) phases.

There is a marked fractionation between light and heavy REEs, with the heavier elements strongly enriched in the aqueous phase (Figure 10.5-2). The heavy REEs show a greater tendency for complexation and a greater affinity for mineral surfaces (Jarvis et al. 1997 [157489]), suggesting association with colloidal particles. Given the degree of fractionation exhibited by the lanthanide series elements (REEs), finely comminuted monazite cannot represent the dominant colloidal phase. Extensive leaching and alteration of the original mineralogy must have occurred and has resulted in a phase or phases containing proportionally more uranium, thorium, and REE than the parent. A similar phenomenon has been observed at other localities where monazite weathering is accompanied by preferential loss of uranium and thorium (Jarvis et al. 1997 [157489], p. 16).

Results of the study indicate that the monazite deposit behaves as a partly open system, especially where monazite disseminated in its silicate matrix is exposed to oxidizing surface and groundwaters along fractures and stratigraphic discontinuities, such as the contact between overburden and bedrock. Under these conditions, there is evidence that colloids in the infiltrating water act as vectors for the transport of thorium, uranium, and REE. This evidence includes very high concentrations of uranium and thorium and fractionation between the heavy and light REE in samples taken from boreholes. Final results of this study are not yet available, but the information to date indicates that both the Steenskampskraal and Nopal I sites are open systems with respect to thorium, with colloidal transport being the main transport mechanism. Both sites are similar to Yucca Mountain with respect to unsaturated, oxidizing conditions. This suggests that should thorium escape waste packages emplaced at Yucca Mountain, it would likely be transported by colloids, unless attenuated by filtration.

### 10.5.2 Koongarra

The Koongarra uranium deposit at Alligator Rivers, Australia is found at the steeply tilted contact between Proterozoic sandstone and schist (CRWMS M&O 2000 [151945], Section 13). The ore body is located in a shallow unsaturated environment that is subject to seasonal fluctuations of monsoons. Payne et al. (1992 [124812]) investigated the role of colloids in transport of uranium in the dispersion fan of the weathered zone above the ore body. The colloids and particles included clay minerals, particularly kaolinite, and chlorite, along with fine quartz grains. Iron was present as particle coatings, and in a separate colloidal form. The amount of  $^{238}\text{U}$  associated with colloids ranged up to 6.5%, whereas the amount of  $^{230}\text{Th}$  associated with colloids ranged from 10% to 85%. However,  $^{230}\text{Th}$  was associated to a much greater extent with larger particles, which are unlikely to be mobile in natural groundwaters. The high  $^{227}\text{Th}/^{230}\text{Th}$  ratio was high in some fractions, indicating that  $^{227}\text{Ac}$  could be present as colloids. Overall, however, there was little colloidal material in these groundwaters, with only iron, uranium, thorium, and actinium showing a significant association with colloids (Payne et al. 1992 [124812], p. 481).

## 10.6 CONCLUSIONS

The hydrogeologic and geochemical setting at Peña Blanca is closely analogous to that at Yucca Mountain, as described in Section 10.4.2 and in CRWMS M&O 2000 [141407]. While the

hydrogeologic and geochemical features at INEEL are less similar to Yucca Mountain, of the contaminated anthropogenic sites initially considered for study, INEEL provided the closest similarity in that it occurs in a fractured porous medium with perched water zones and units of varying permeability. It provided the additional advantage of data sets that included radionuclides, which strengthen model testing aspects of the analogue study. Radionuclide transport in the surficial sediment zone at the RWMC can be interpreted in a number of ways. One is that lateral flow occurred, sweeping out part of the radionuclide plume. The thickness of the stratigraphic layers is highly irregular, and the possibility exists that flow occurred along the interface between the clay layer and the surficial sediment layer. This would be in keeping with the hypothesis of Nimmo et al. 2001 [154458]). Another possibility is that a catastrophic or sudden release of a pulse of fluid caused by a flooding event released a pulse of radionuclides that propagated downward with reduced retardation, owing to kinetic effects in turn caused by fast flow rates. Presumably, according to this interpretation, the concentration peak lies at a still greater depth below that at which the data were collected.

The model calculations predict retardation factors for neptunium and uranium that are seen to be orders of magnitude higher compared to the other radionuclides. This result would indicate that very little movement of neptunium and uranium should be observed. No values for these radionuclides were reported that could be taken as consistent with their predicted high retardation.

In comparison to Yucca Mountain, the wetter environment at INEEL is manifested in higher infiltration at the SDA and flooding events that could have resulted in enhanced radionuclide migration beneath the SDA. Focused flow, resulting from the undulating topography of the basalt flows and sedimentary interbeds, would be expected to exacerbate the situation, leading to even greater distances of radionuclide migration, as demonstrated in the modeling exercises. The UZ Flow and Transport Model at Yucca Mountain considers a range of infiltration rates that are then used to bound the range of percolation flux. Because the PTn has a damping effect on flow to the TSw, it is unlikely that the enhanced transport scenario proposed in the INEEL modeling study would occur at Yucca Mountain.

At Nopal I, the evolution of stable isotopes for the adit samples appears to have at least three components: (1) evolution of vapor from the GMWL, (2) modification by water/rock interaction, and (3) evaporation in the adit collection system. A simpler approach planned for evaluation shortly is to normalize the uranium data to chloride or bromide concentrations. It is estimated that the transit time for the seep water that infiltrated into the Nopal I Level +00 adit 8 m below surface is about 6–29 days, and for the perched water at 10.7 m depth in an old borehole, the transit time is about 0.4–0.5 years. The large values of  $\tau_w$  for the perched water may reflect the long residence time of water in the borehole. It should be noted that as water at different sites may have different pathways, the value of  $\tau_w$  itself does not provide information on possible connections between the perched and seep waters sampled. In conclusion, although the water transit time in the UZ is quite short, significant dissolution of uranium may have occurred in a low-water flux, high-uranium concentration setting near the Nopal I uranium deposit. If analyses from future sampling campaigns confirm that transit time is short in the UZ at Nopal I, then the implications would need to be considered for the similar low-water flux environment at Yucca Mountain.

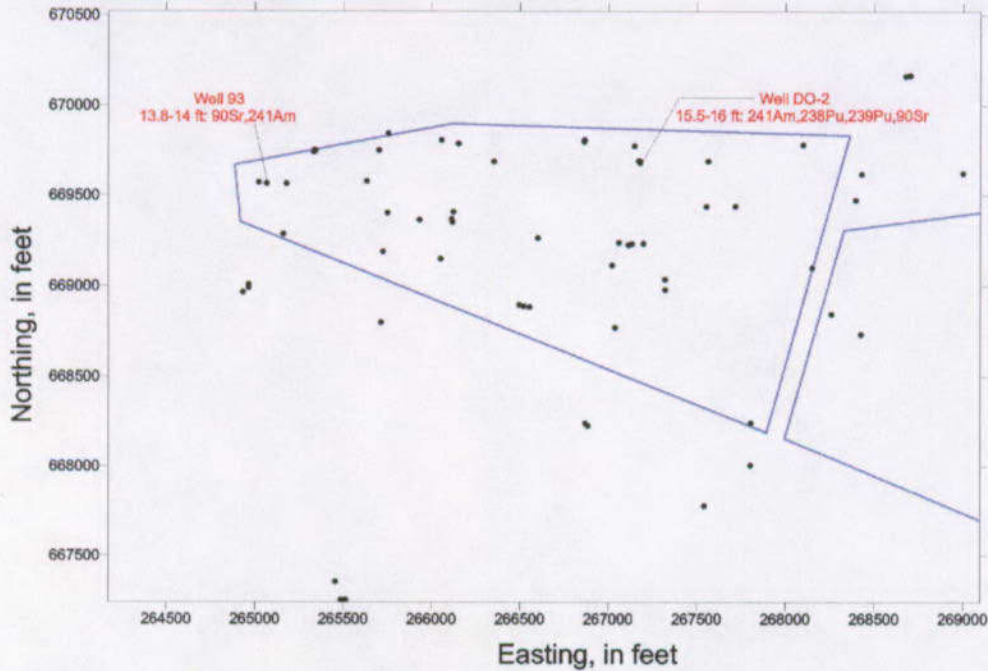
Compared with samples collected during the September wet season of 1995, many of the new measurements in late February 2000, and again in early March 2001, show much higher  $^{238}\text{U}$  concentration and lower  $^{234}\text{U}/^{238}\text{U}$ , suggesting increased uranium dissolution and/or lower  $\alpha$ -recoil-associated  $^{234}\text{U}$  enrichment rates during the dry seasons. The low humidity during dry seasons may have also enhanced evaporation, causing higher uranium concentrations in the waters sampled.

The data collected during the winter dry seasons of 2000 and 2001 depart considerably from the linear relationship between  $^{234}\text{U}/^{238}\text{U}$  and  $1/^{238}\text{U}$  predicted by the model for the wet season of 1995 (Figure 10.4-5a). Such a departure could be caused by: (1) high and variable evaporation under low humidity conditions, and (2) incomplete flushing associated with low rainfall during the dry season. The uranium dissolution rates are about three times higher than those in the wet season, possibly suggesting a favorable physiochemical condition (e.g., increased oxygenation) for uranium dissolution during dry periods.

Large variations in the  $^{238}\text{U}$  concentration and  $^{234}\text{U}/^{238}\text{U}$  ratio were also found in samples collected from the SZ during the dry season. Both the decreased water infiltration flux and the increased uranium dissolution rates in the vadose zone may contribute to the higher dry-season uranium concentrations in the SZ. Observations such as these may have important implications for the effects of climate change on the long-term stability of uranium in the environment.

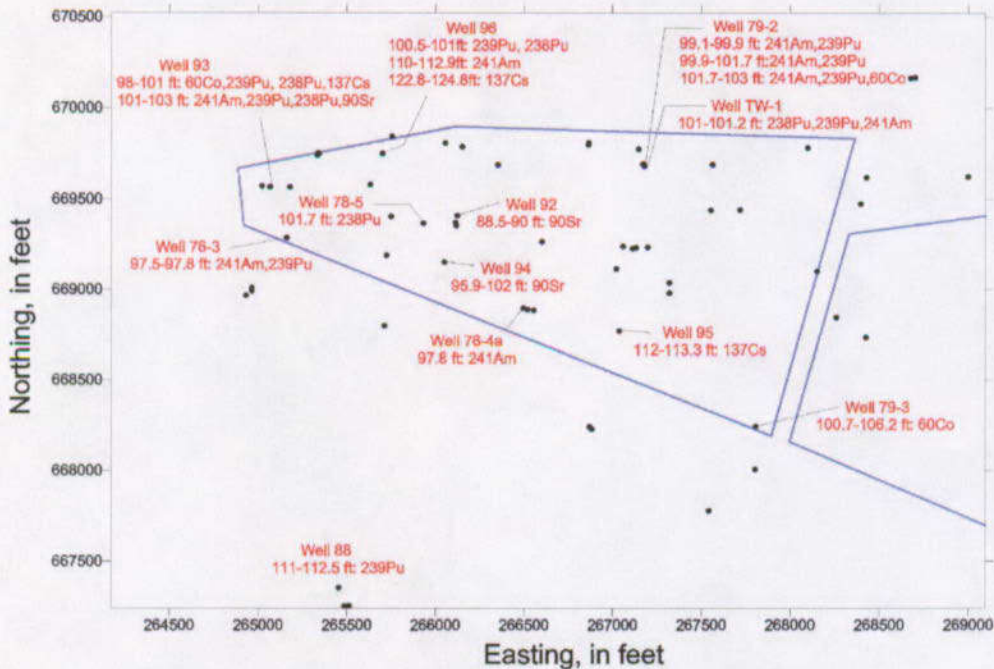
As a final point, colloid transport appears to be an important factor for migration of thorium in one open unsaturated system, Steenkampskraal, but not in another, Nopal I. Both systems have similar hydrologic conditions to those at Yucca Mountain, although the rock type is different at Steenkampskraal. At Koongarra, another unsaturated but seasonally fluctuating system, colloid transport takes place but is a minor mechanism of uranium transport. Because seasonal fluctuations in uranium dissolution have been discovered at Nopal I, it would be useful to investigate the possibility of colloid transport in that system. A more informed understanding of the implication for colloid transport in the UZ at Yucca Mountain could then be had and could be used to evaluate whether TSPA assumptions that disregard colloid filtration are appropriately conservative.





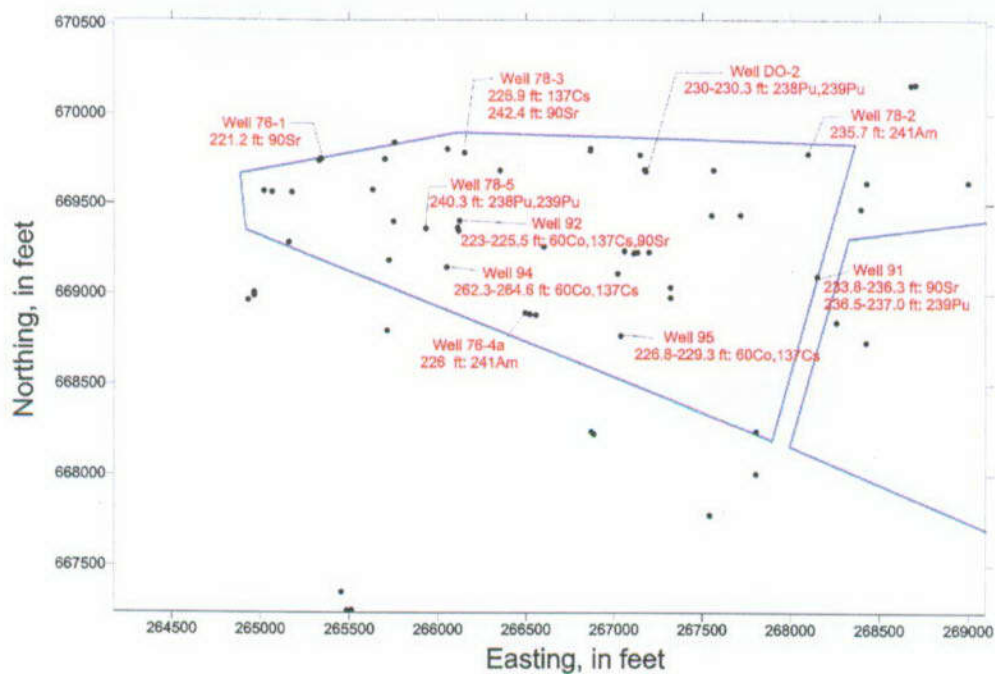
Source: Simmons 2002 [157578], SN-LANL-SCI-234-V1, p. 61.

Figure 10.3-1a. Map of SDA and Deep Wells Showing Location of Radionuclide Concentrations Greater Than Three Times Detection for Depth Intervals to the 9 m Interbed



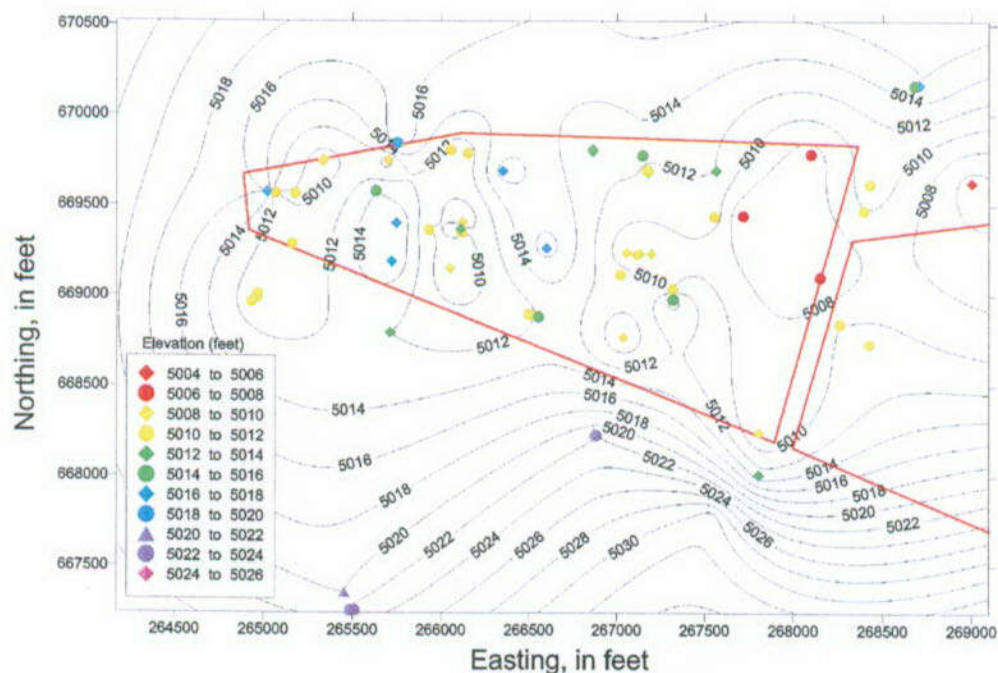
Source: Simmons 2002 [157578], SN-LANL-SCI-234-V1, p. 61.

Figure 10.3-1b. Map of SDA and Deep Wells Showing Location of Radionuclide Concentrations Greater Than Three Times Detection for Depth Intervals to the 34 m Interbed



Source: Simmons 2002 [157578], SN-LANL-SCI-234-V1, p. 62.

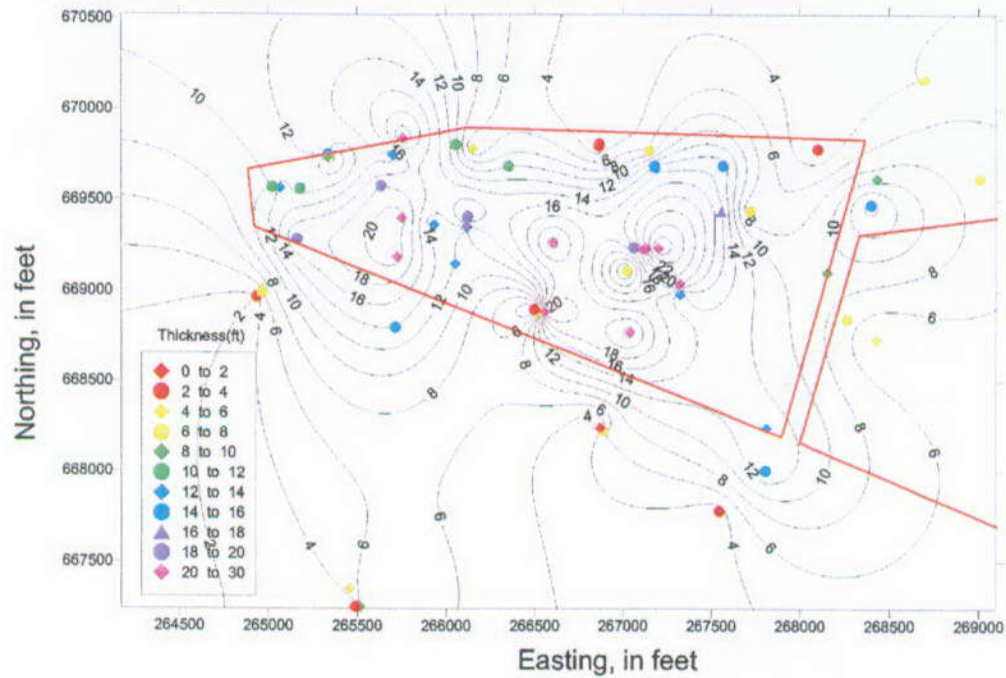
Figure 10.3-1c. Map of SDA and Deep Wells Showing Location of Radionuclide Concentrations Greater Than Three Times Detection for Depth Intervals to the 73 m Interbed



Source: Simmons 2002 [157578], SN-LANL-SCI-234-V1, p. 63.

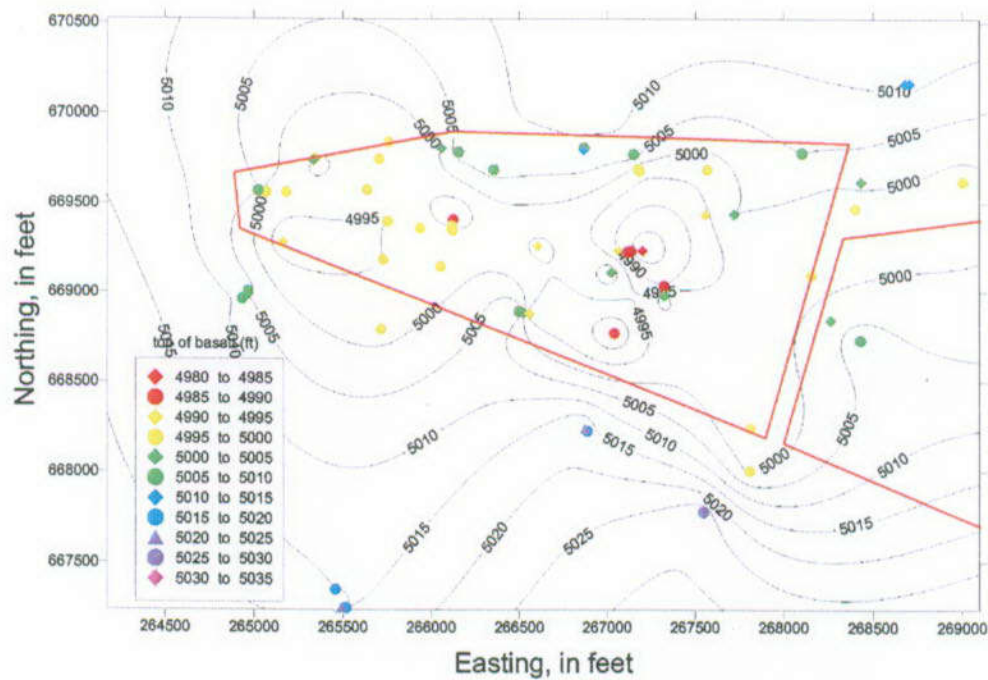
Figure 10.3-2. Ground Surface Elevation in the Vicinity of the SDA





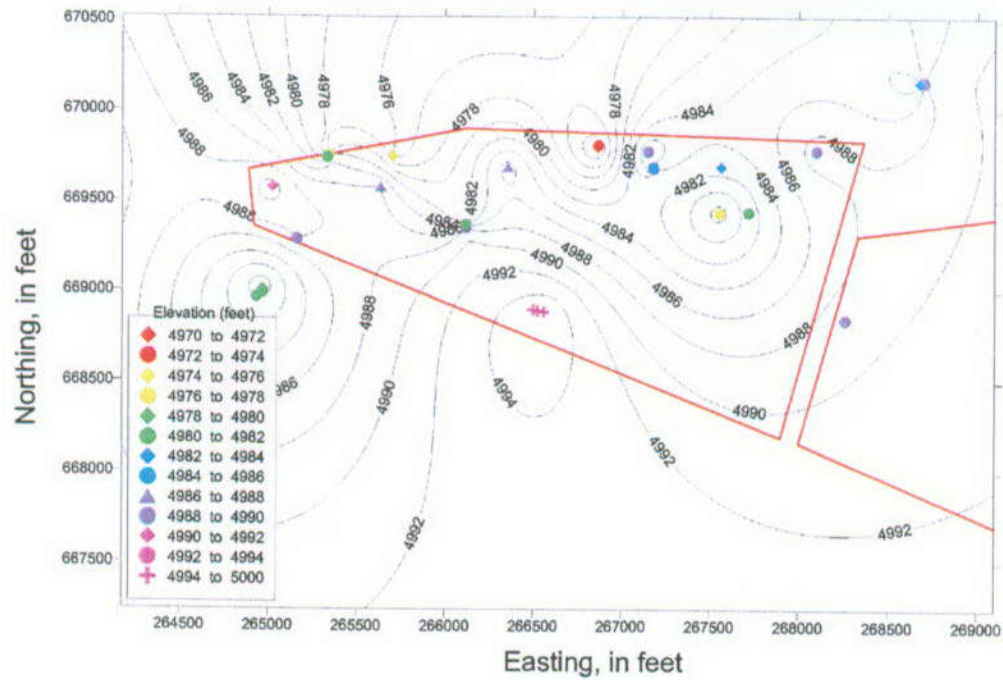
Source: Simmons 2002 [157578], SN-LANL-SCI-234-V1, p. 64.

Figure 10.3-3. Surficial Sediment Thickness in the Vicinity of the SDA



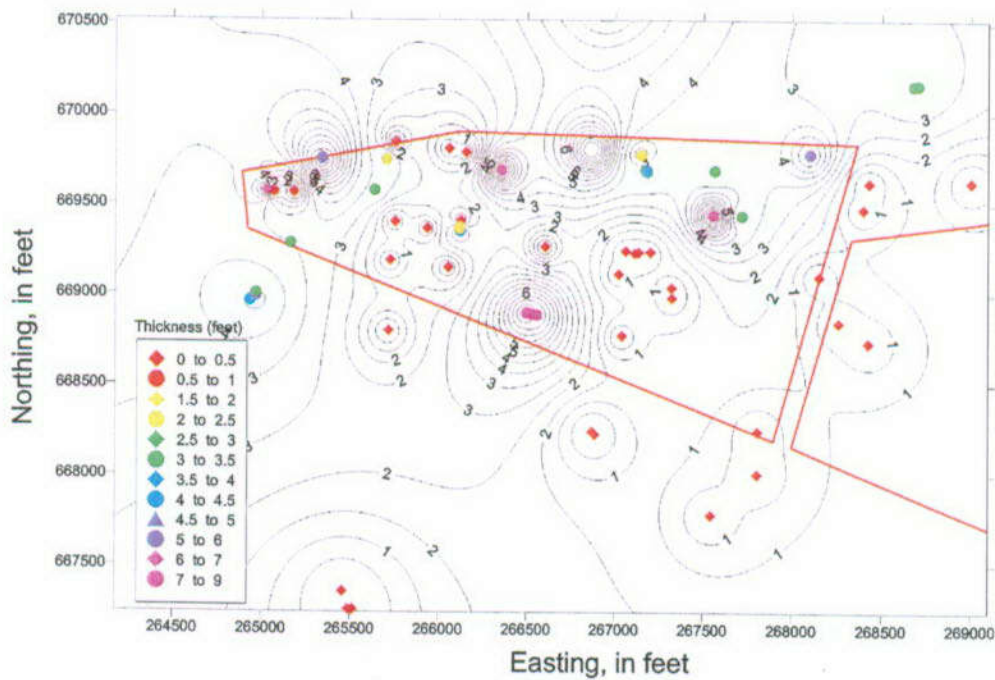
Source: Simmons 2002 [157578], SN-LANL-SCI-234-V1, p. 64.

Figure 10.3-4. Elevation of Top of Basalt Flow A in the Vicinity of the SDA



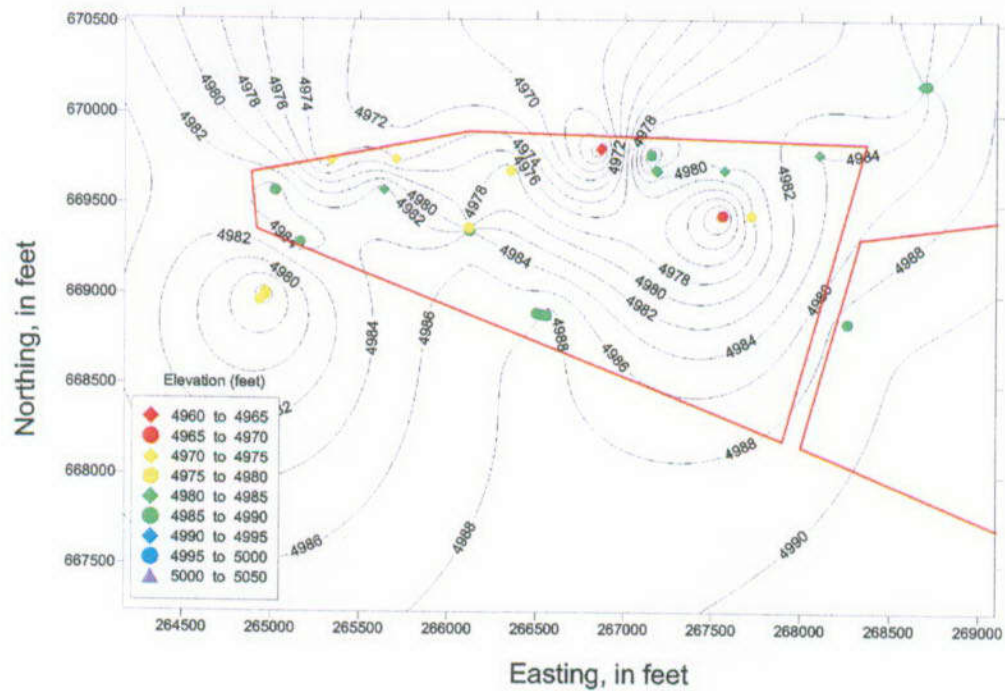
Source: Simmons 2002 [157578], SN-LANL-SCI-234-V1, p. 65.

Figure 10.3-5. Elevation of Top of AB Interbed in the Vicinity of the SDA



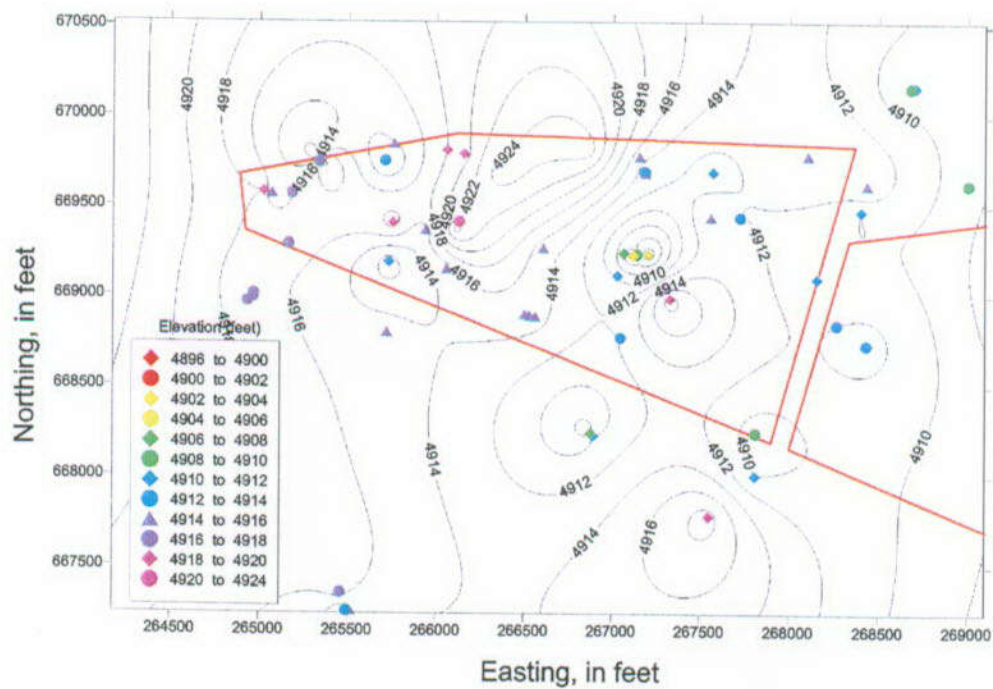
Source: Simmons 2002 [157578], SN-LANL-SCI-234-V1, p. 65.

Figure 10.3-6. Thickness of AB Interbed in the Vicinity of the SDA



Source: Simmons 2002 [157578], SN-LANL-SCI-234-V1, p. 66.

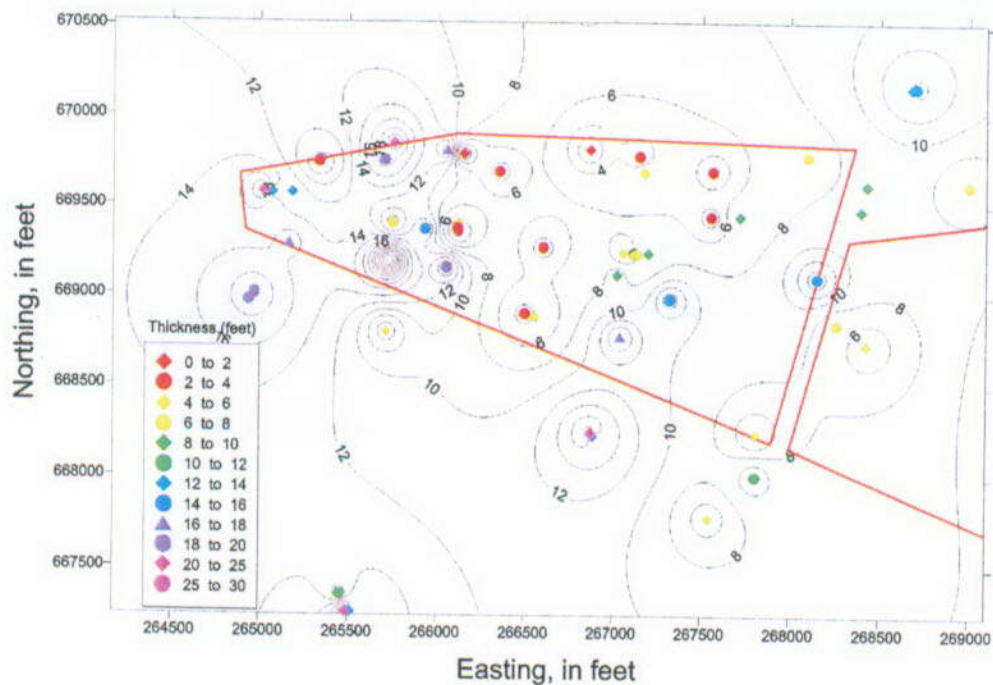
Figure 10.3-7. Elevation of Top of B Basalt in the Vicinity of the SDA



Source: Simmons 2002 [157578], SN-LANL-SCI-234-V1, p. 66.

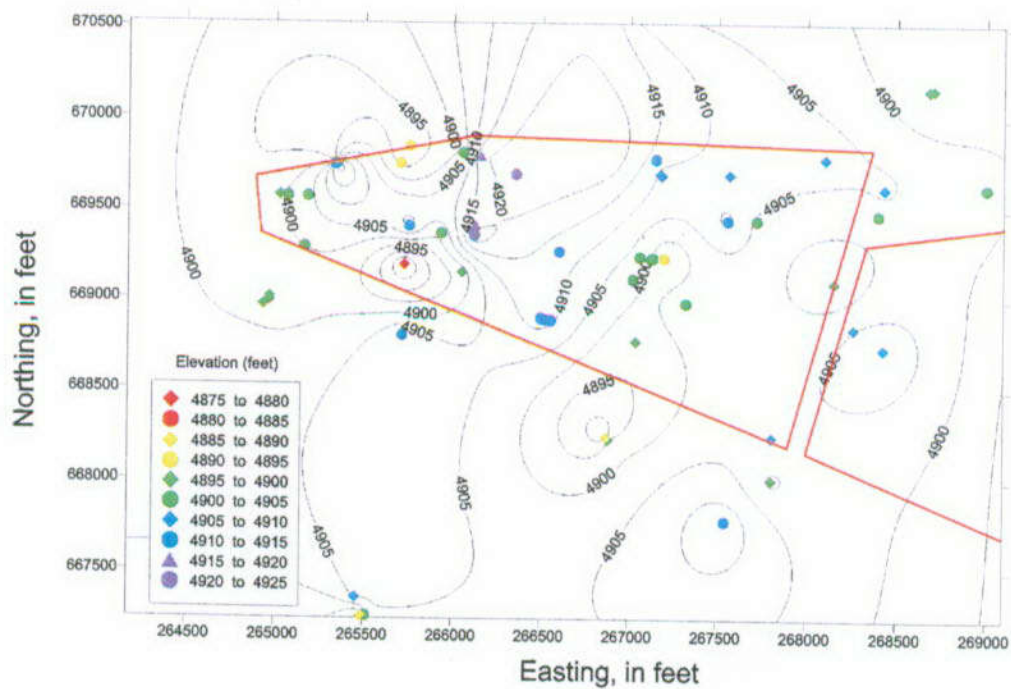
Figure 10.3-8. Elevation of Top of BC Interbed in the Vicinity of the SDA





Source: Simmons 2002 [157578], SN-LANL-SCI-234-V1, p. 67.

Figure 10.3-9. Thickness of BC Interbed in the Vicinity of the SDA



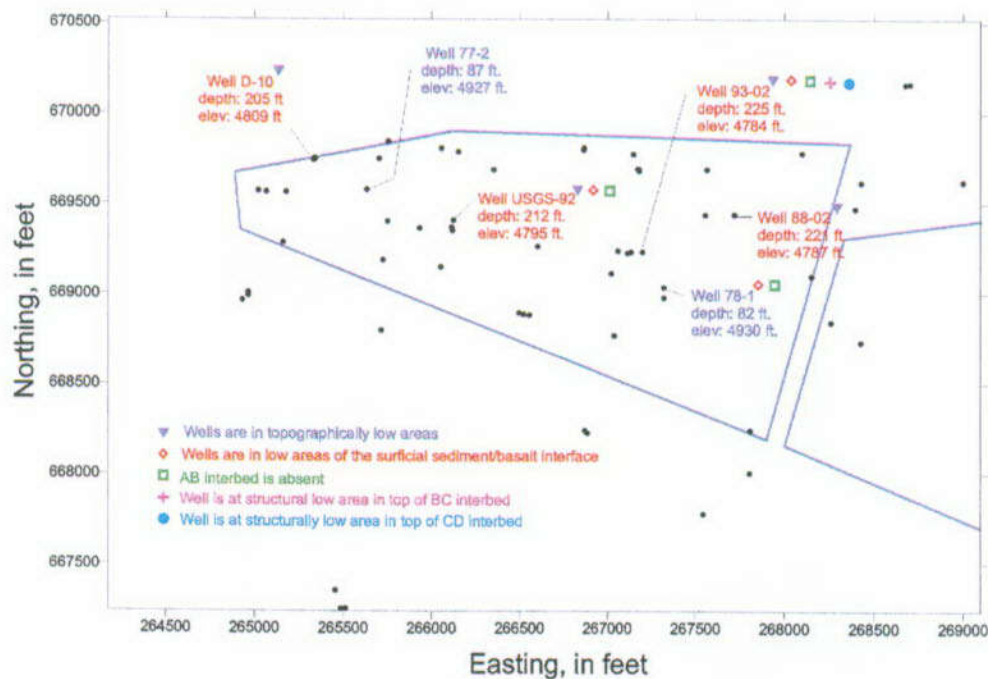
Source: Simmons 2002 [157578], SN-LANL-SCI-234-V1, p. 67.

Figure 10.3-10. Elevation of Top of C Basalt in the Vicinity of the SDA



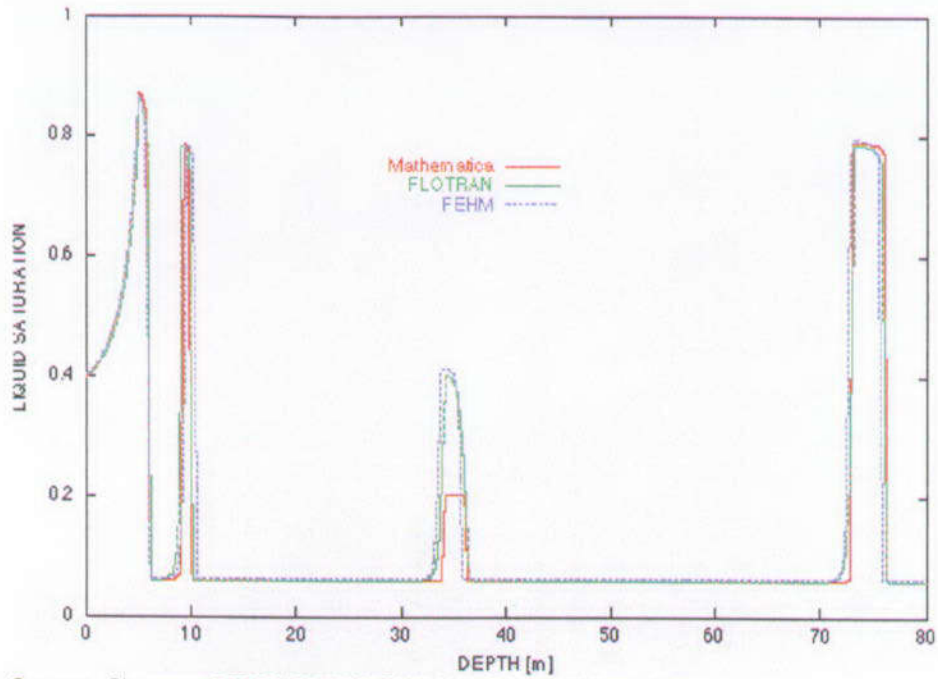
Source: Simmons 2002 [157578], SN-LANL-SCI-234-V1, p. 68.

Figure 10.3-11. Elevation of Top of CD Interbed in the Vicinity of the SDA



Source: Simmons 2002 [157578], SN-LANL-SCI-234-V1, p. 75.

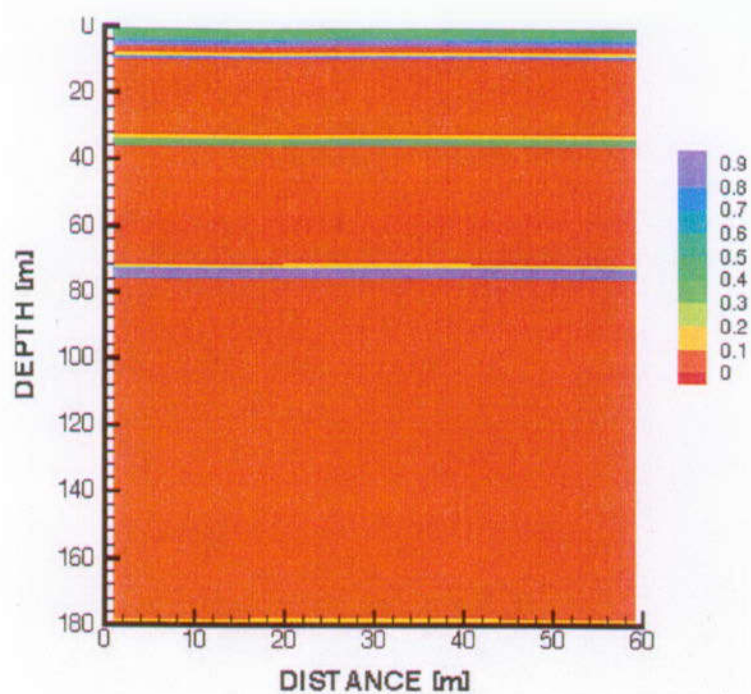
Figure 10.3-12. Depths and Elevations of Perched Water in the Vicinity of the SDA



Source: Simmons 2002 [157578], SN-LANL-SCI-234-V1, p. 16.

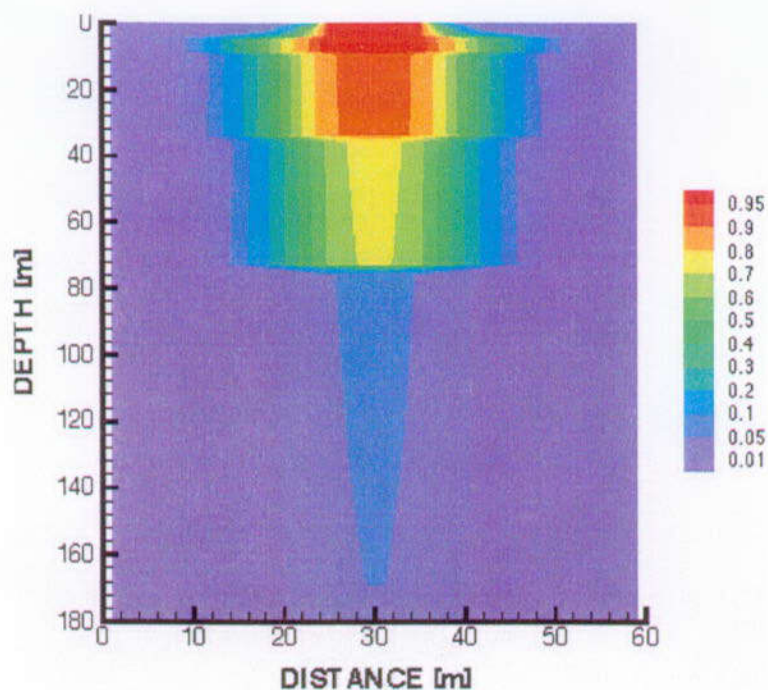
Figure 10.3-13. Comparison of Steady-State Saturation Profiles for FEHM and FLOTRAN for Single-Continuum Simulation





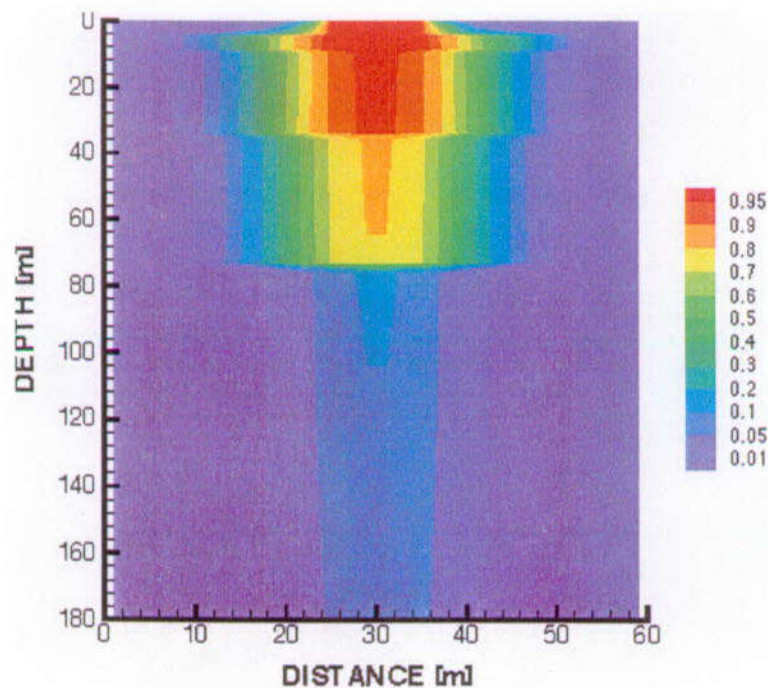
Source: Simmons 2002 [157578], SN-LANL-SCI-234-V1, p. 20.

Figure 10.3-14. Liquid Saturation for the Single-Continuum Simulation



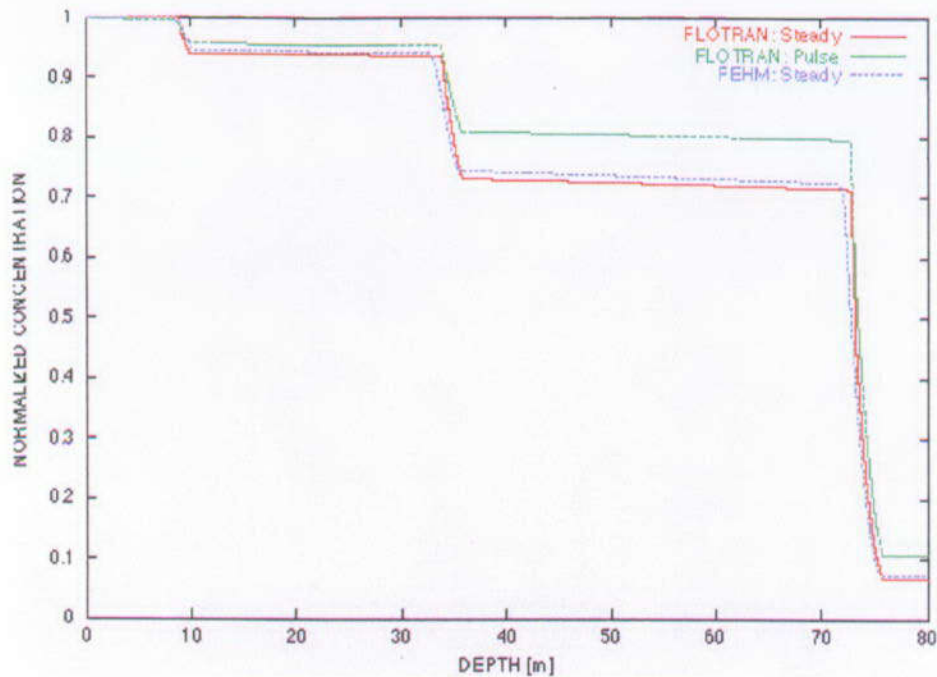
Source: Simmons 2002 [157578], SN-LANL-SCI-234-V1, p. 23.

Figure 10.3-15a. Normalized Tracer Concentration after 50 Years for the Single-Continuum Model with Constant Release



Source: Simmons 2002 [157578], SN-LANL-SCI-234-V1, p. 23.

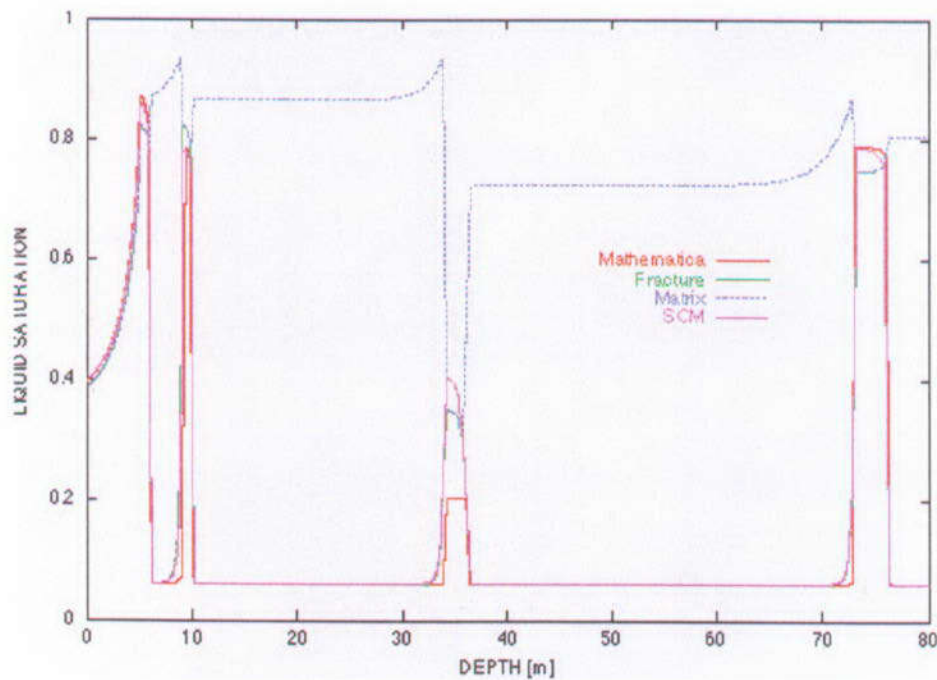
Figure 10.3-15b. Normalized Tracer Concentration after 50 years for the Single-Continuum Model with Pulse Release



NOTE: Also Shown is the Pulse Release using FLOTRAN.

Source: Simmons 2002 [157578], SN-LANL-SCI-234-V1, p. 24.

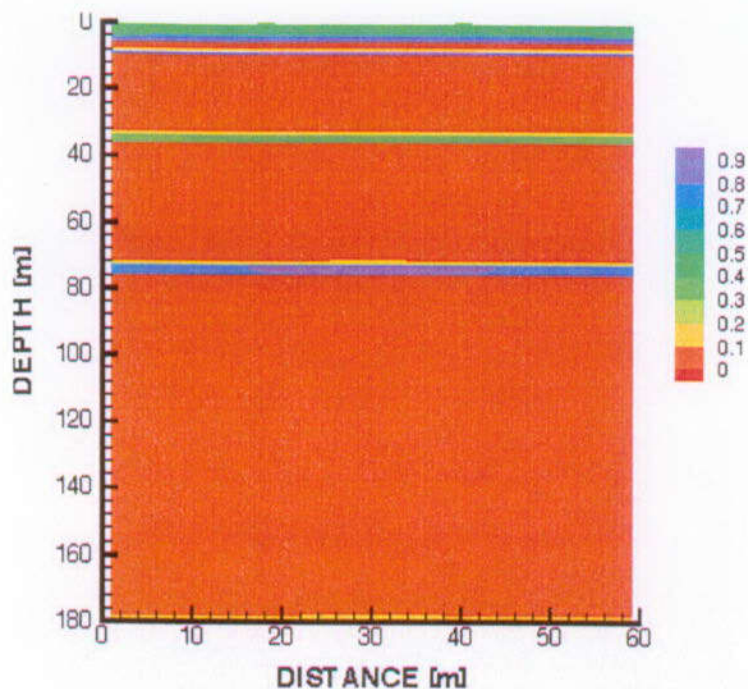
Figure 10.3-16. Comparison of FEHM and FLOTRAN for Normalized Tracer Concentration after 50 Years for the Single-Continuum Model with Steady Release at the Center of the Injection Region



Source: Simmons 2002 [157578], SN-LANL-SCI-234-V1, p. 24.

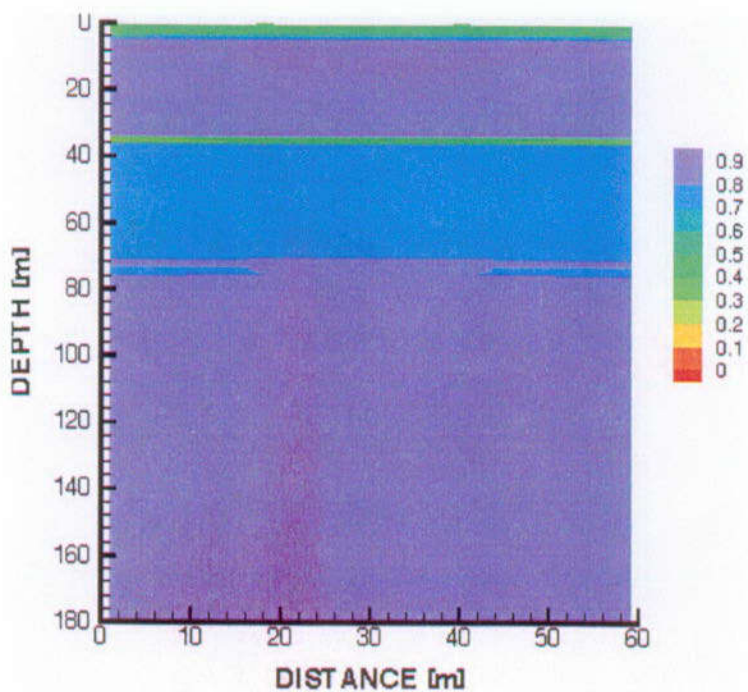
Figure 10.3-17. Comparison of Steady-State Saturation Profiles for Single- and Dual-Continuum Simulations





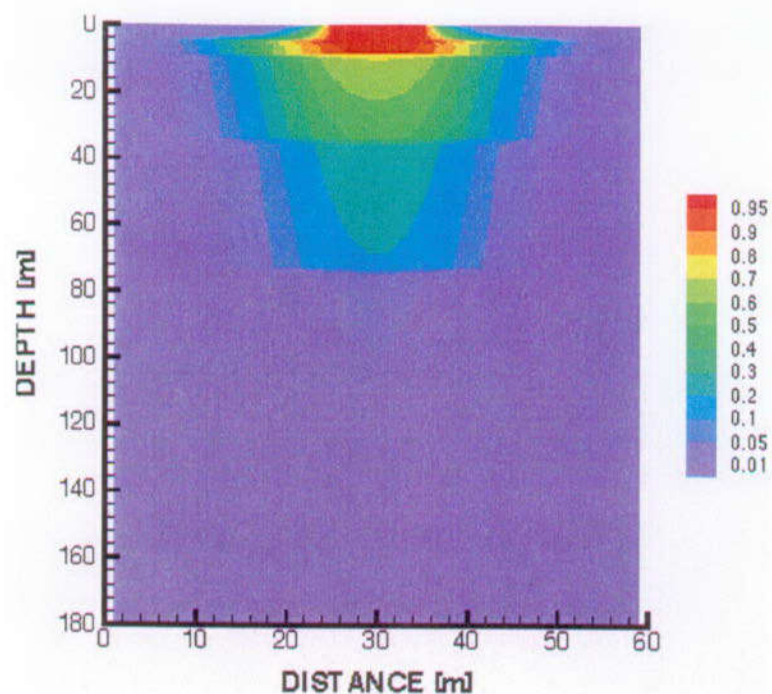
Source: Simmons 2002 [157578], SN-LANL-SCI-234-V1, p. 26.

Figure 10.3-18a. Liquid Saturation for Fracture Continuum



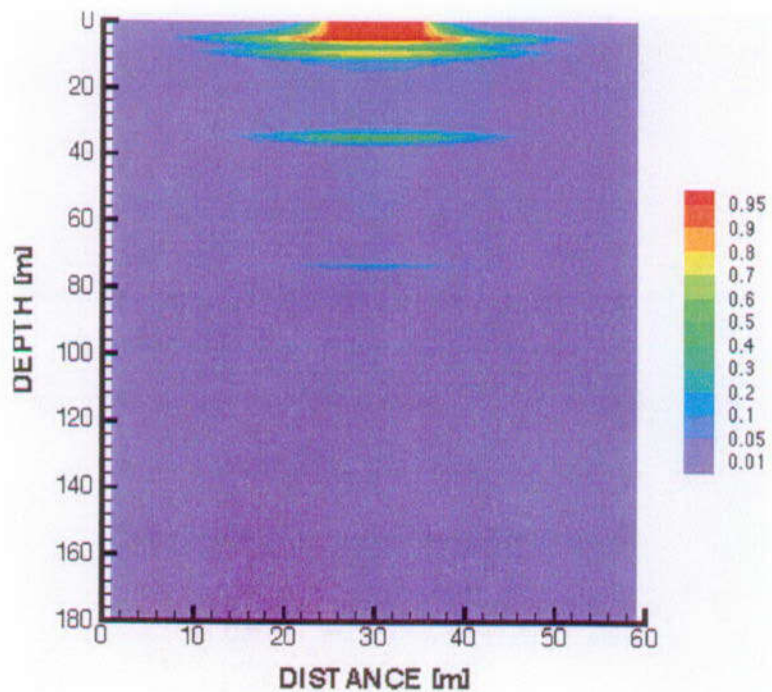
Source: Simmons 2002 [157578], SN-LANL-SCI-234-V1, p. 26.

Figure 10.3-18b. Liquid Saturation for Matrix Continuum



Source: Simmons 2002 [157578], SN-LANL-SCI-234-V1, p. 27.

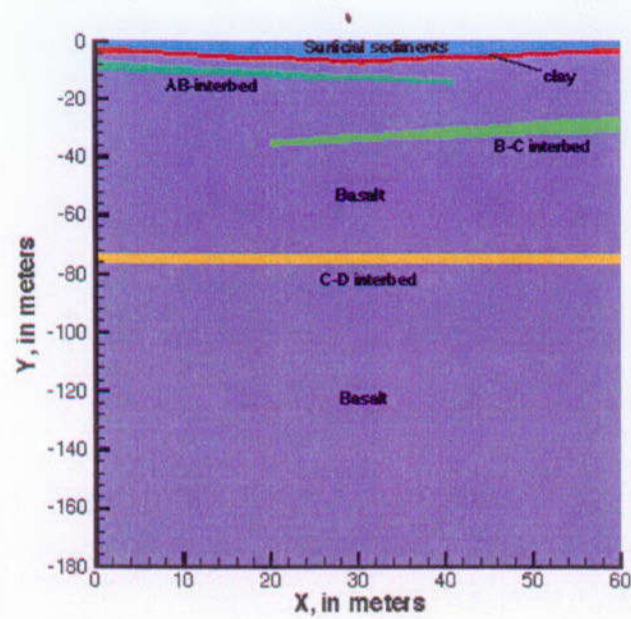
Figure 10.3-19a. Normalized Tracer Concentration for Fracture Continuum



Source: Simmons 2002 [157578], SN-LANL-SCI-234-V1, p. 27.

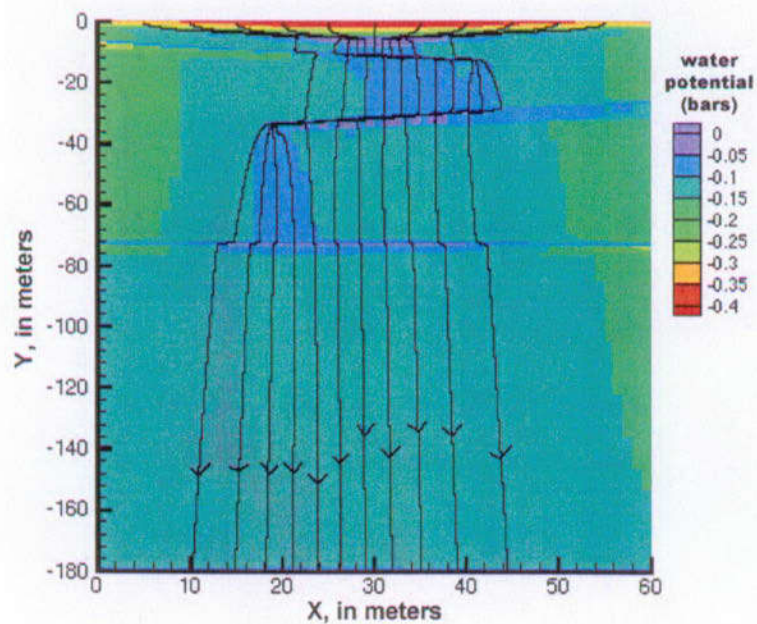
Figure 10.3-19b. Normalized Tracer Concentration for Matrix Continuum





Source: Simmons 2002 [157578], SN-LANL-SCI-234-V1, p. 76.

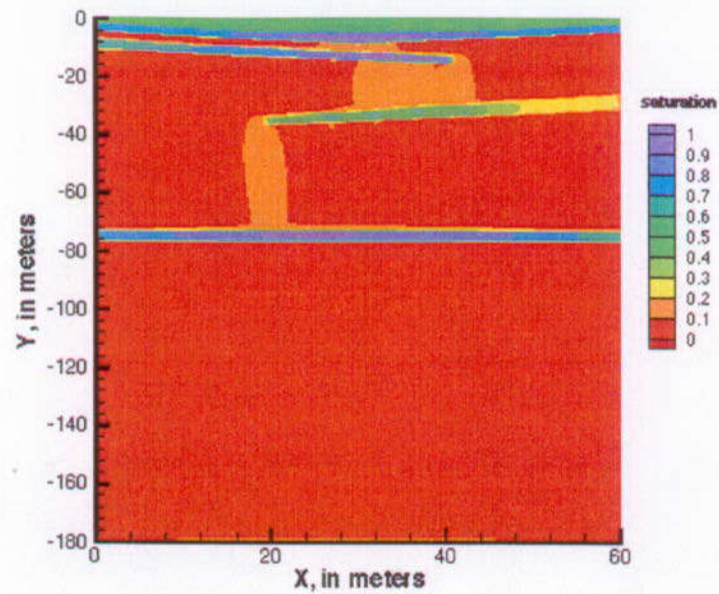
Figure 10.3-20. Hydrostratigraphy



NOTE: Arrows indicate particle-tracking flow lines.

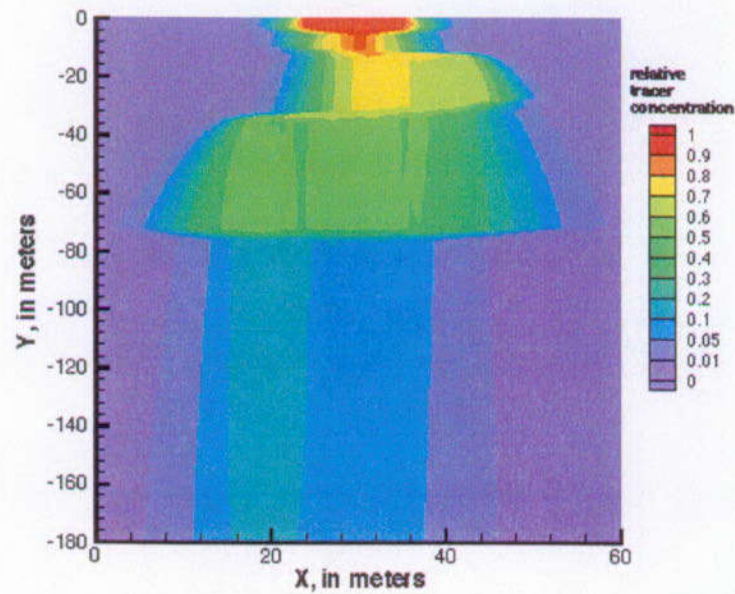
Source: Simmons 2002 [157578], SN-LANL-SCI-234-V1, p. 83.

Figure 10.3-21. Steady-State Water Potentials



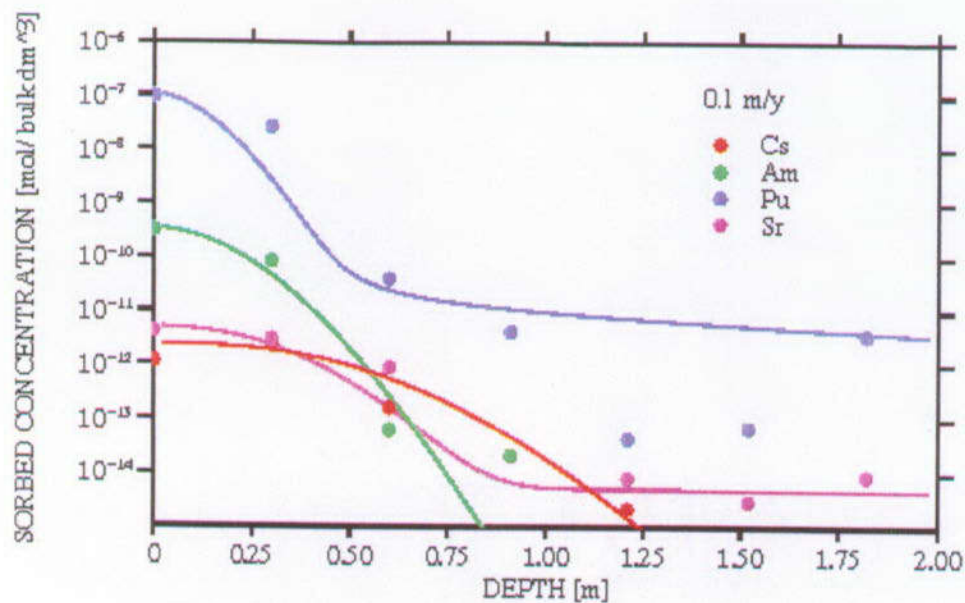
Source: Simmons 2002 [157578], SN-LANL-SCI-234-V1, p. 88.

Figure 10.3-22. Liquid Saturation at 50 Years



Source: Simmons 2002 [157578], SN-LANL-SCI-234-V1, p. 89.

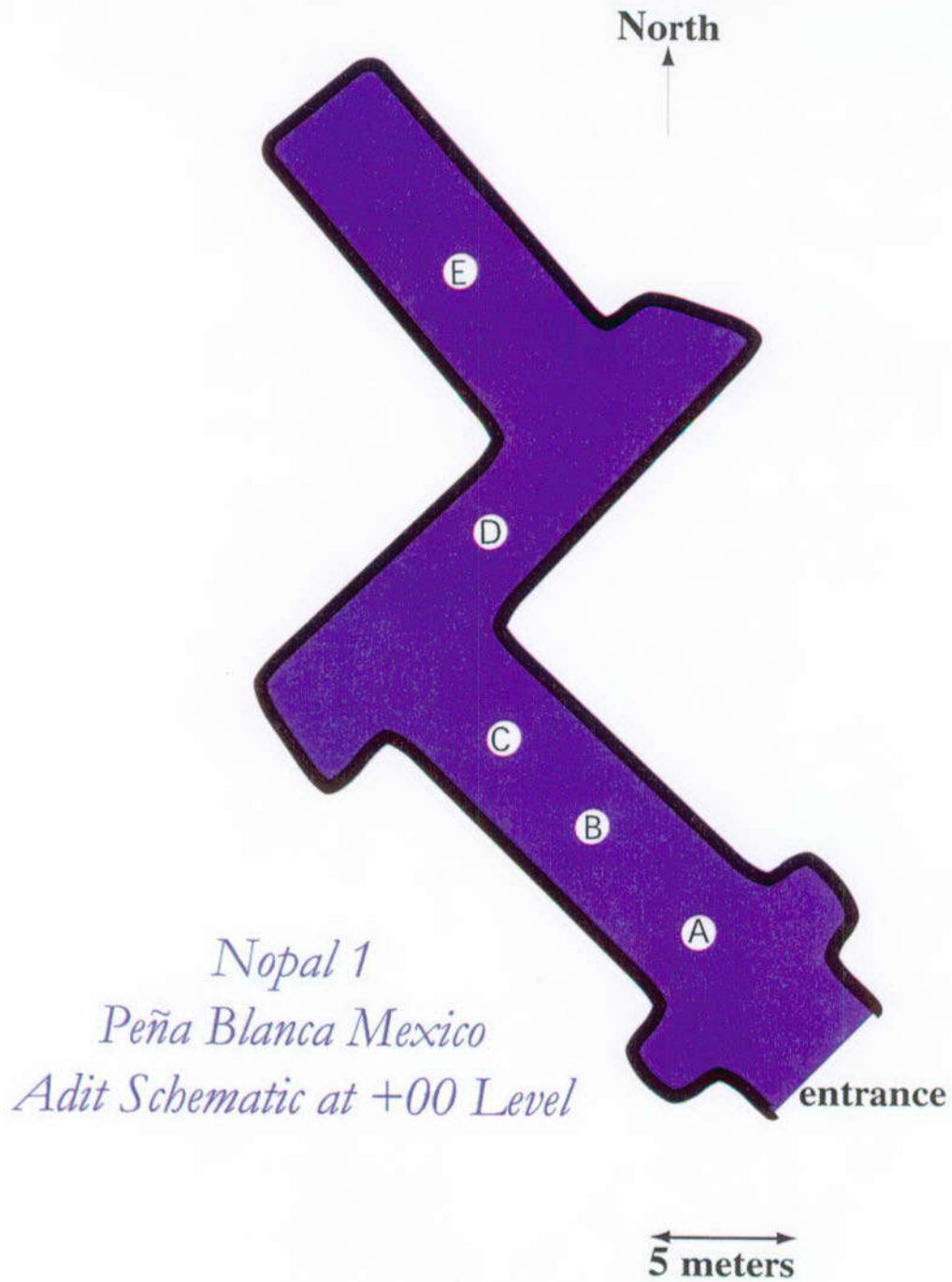
Figure 10.3-23. Normalized Tracer Concentration at 50 Years



Source: Simmons 2002 [157578], SN-LANL-SCI-234-V1, p. 30.

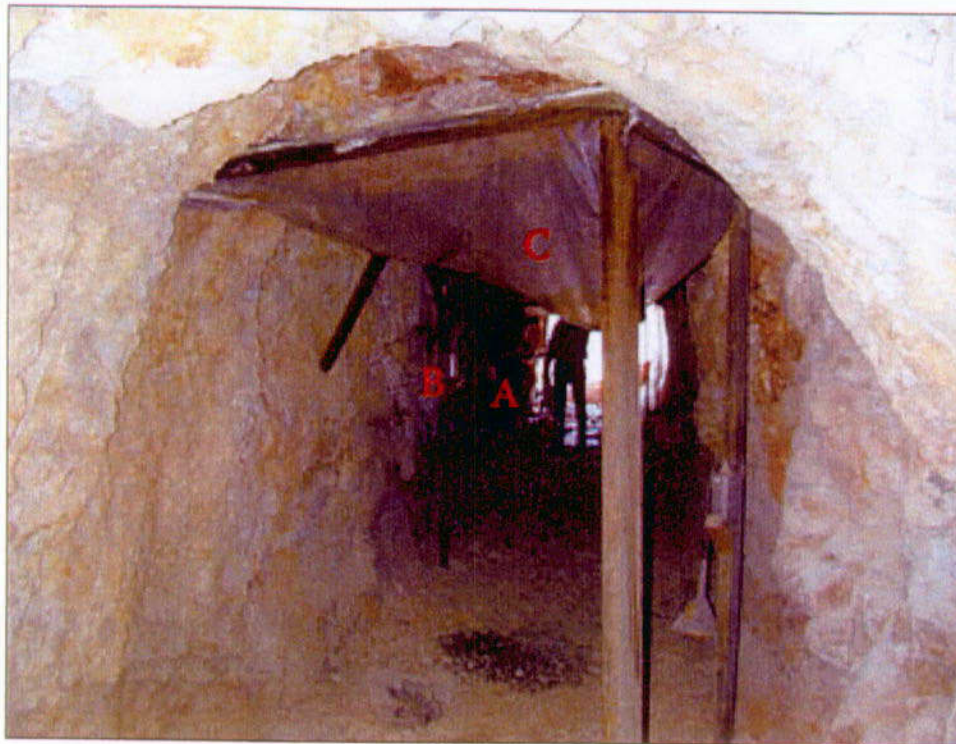
Figure 10.3-24. Comparison of Field Data for Sorption of Cs, Pu, Am, and Sr for a Flow Velocity of 0.1 m/yr through the Surficial Sediment





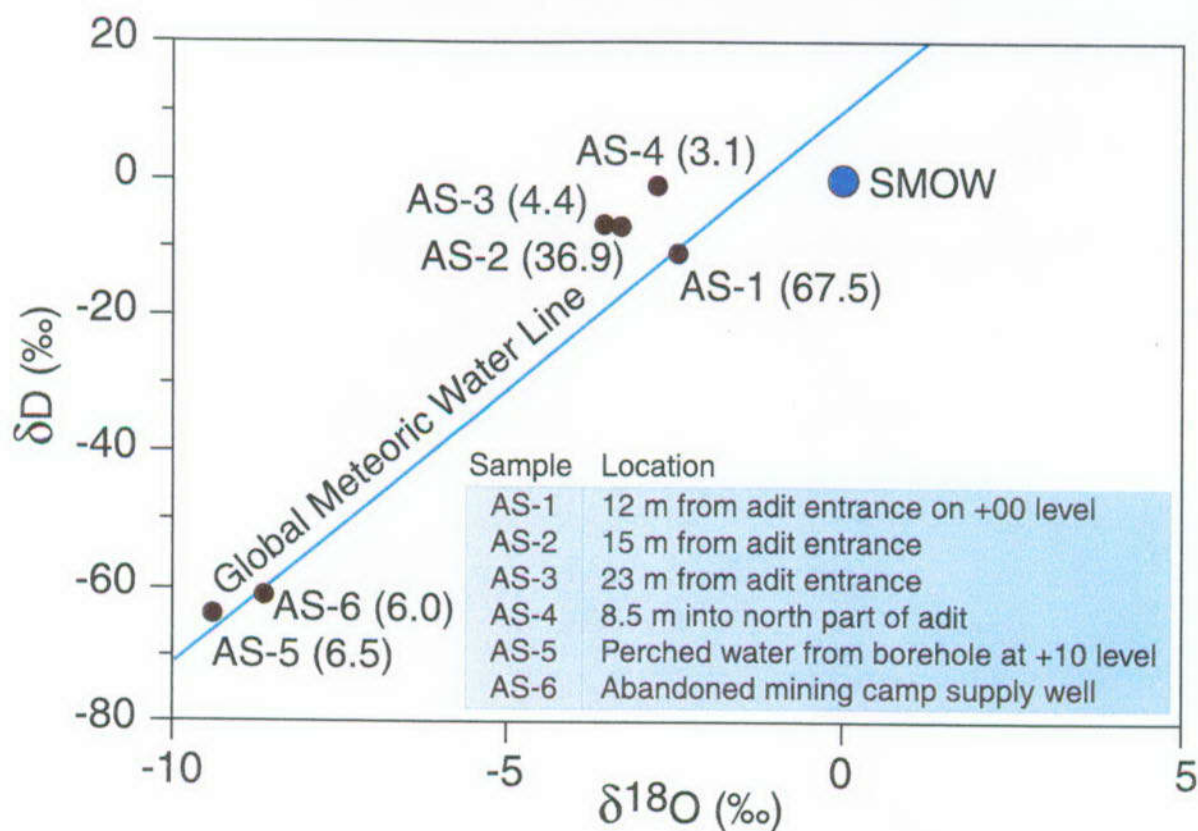
DTN: LB0202PBANALOG.001 [157610]

Figure 10.4-1. Schematic of Level +00 Adit Sampling Locations



DTN: LB0202PBANALOG.001 [157610]

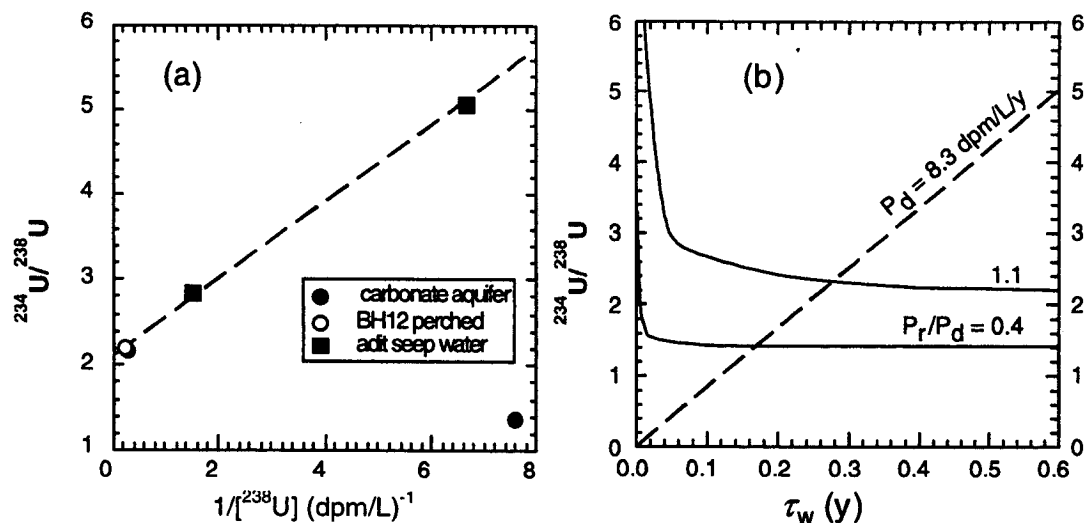
Figure 10.4-2. Photo of Sampling Locations A, B, and C in the Nopal I +00 Adit



DTN: LB0202PBANALOG.001 [157610]

NOTE: Also shown is the position of the global meteoric water line and SMOW (Standard Mean Ocean Water).

Figure 10.4-3. Plot of  $\delta D$  versus  $\delta^{18}O$  for water samples collected (black circles) from Peña Blanca during February 2000

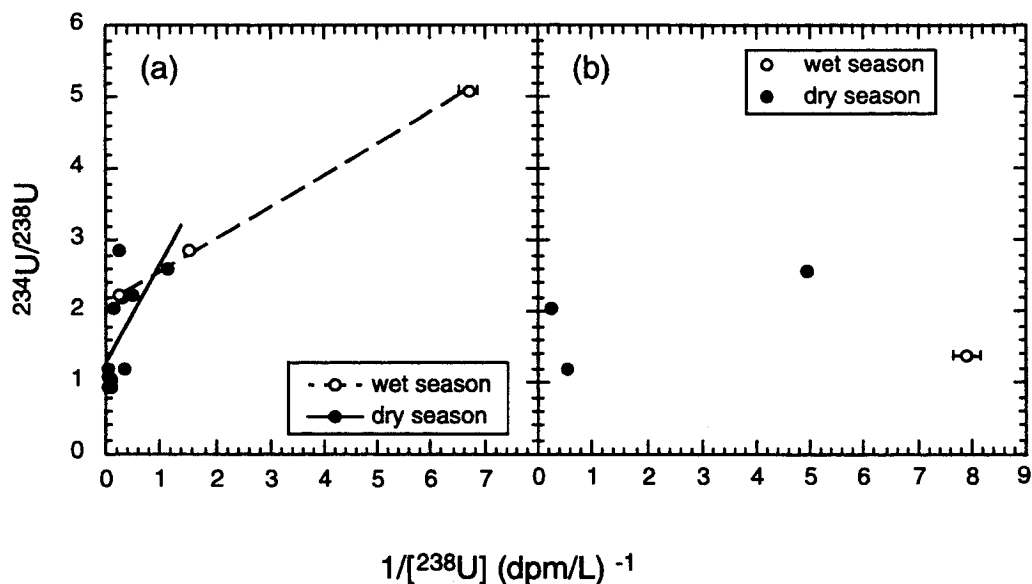


NOTE: The dashed line in (a) delineates the positive linear correlation for waters sampled from the UZ. Its slope and intercept can be used to derive  $P_r$  (input from recoil) and  $P_d$  (input from dissolution) by the model. (b) shows a rapid decrease of  $^{234}\text{U}/^{238}\text{U}$  to a relatively constant level within a couple of weeks after the water enters the UZ. The low  $^{234}\text{U}/^{238}\text{U}$  activity ratio of 1.39 in the carbonate aquifer as shown in (a) requires a  $P_r/P_d$  ratio of about 0.4, about three times smaller than that in the UZ.

(dpm/L) $^{-1}$  values calculated from data in Table 10.4-1, using half-lives of  $^{234}\text{U}$  and  $^{238}\text{U}$ .

Source: Modified from Pickett and Murphy 1999 [110009], Figure 15.

Figure 10.4-4. (a)  $^{234}\text{U}/^{238}\text{U}$  Activity Ratio vs. Reciprocal  $^{238}\text{U}$  Activity in Nopal I Waters and (b)  $^{234}\text{U}/^{238}\text{U}$  Activity Ratio (solid lines) and  $^{238}\text{U}$  Concentration (dashed line) as a Function of Water Transit Time ( $\tau_w$ ) in the UZ



NOTE: Solid and dashed lines in (a) are linear regressions for samples collected during the dry (February 2000 and March 2001 collections) and wet (August - September of 1995) seasons, respectively. Dissolution of uranium is higher during the dry periods.

Source: Data values calculated from data in Table 10.4-1, using half-lives of  $^{234}\text{U}$  and  $^{238}\text{U}$ .

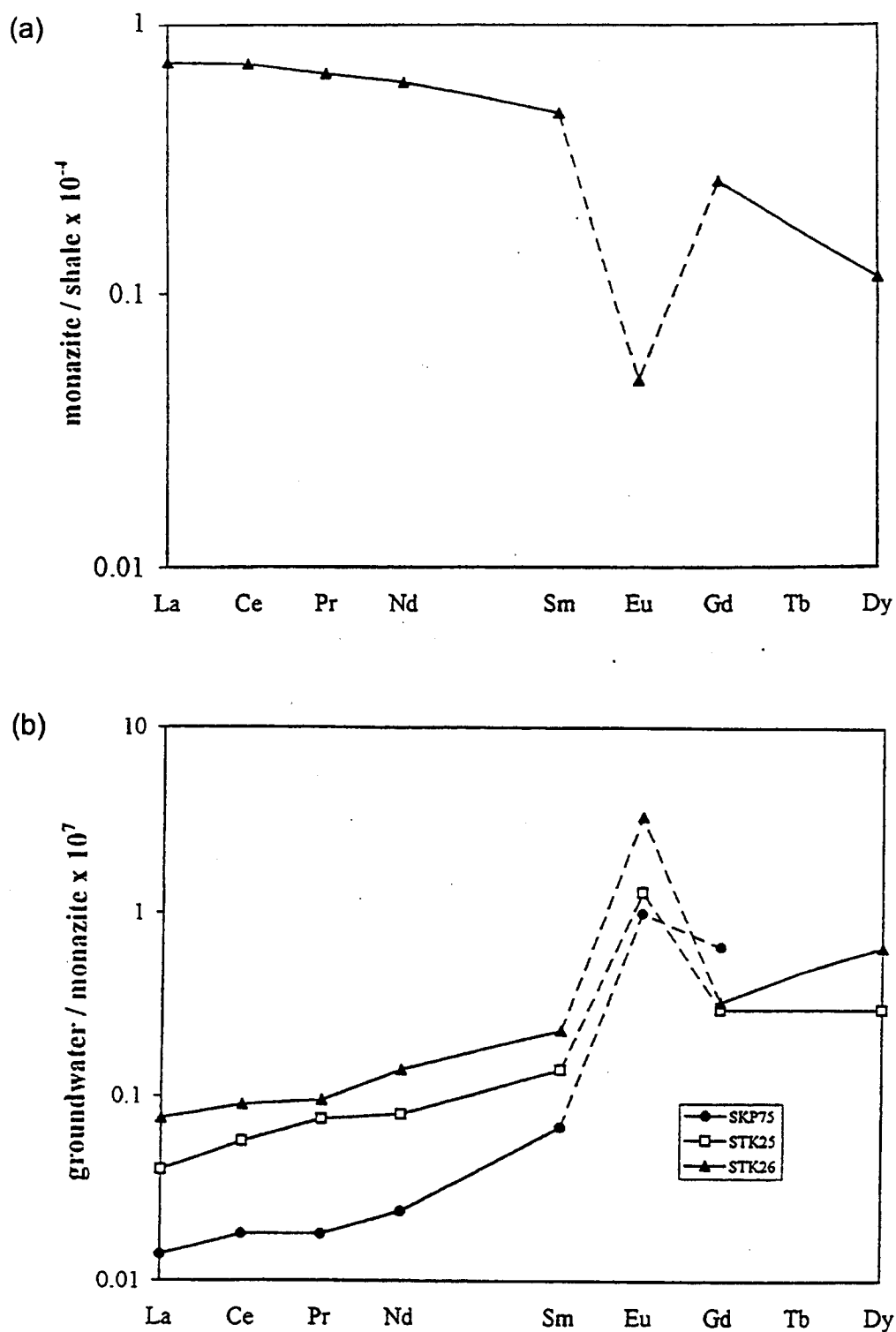
Figure 10.4-5.  $^{234}\text{U}/^{238}\text{U}$  Activity Ratio vs. Reciprocal  $^{238}\text{U}$  Activity in Nopal I Waters from (a) UZ and (b) SZ





Source: Jarvis et al. 1997 [157489], Figure 1.

Figure 10.5-1. Location of Steenkampskraal, South Africa



Source: Jarvis et al. 1997 [157489], Figures 3 and 4.

Figure 10.5-2. (a) Shale-normalized REE Pattern for Steenkampskraal Monazites and (b) REE Distribution for Groundwater Samples Normalized to Average Steenkampskraal Monazite

Table 10.3-1. Chemical Characteristics of Selected Samples of Pore Water, Perched Water, and Groundwater from Yucca Mountain and the Subsurface Disposal Area of INEEL

Location	Temp. (°C)	pH	Ca (mg/L)	Mg (mg/L)	Na (mg/L)	K (mg/L)	Cl (mg/L)	SO <sub>4</sub> (mg/L)	HCO <sub>3</sub> (mg/L)	SiO <sub>2</sub> (mg/L)	F (mg/L)	NO <sub>3</sub> (mg/L)	Data Source
Yucca Mountain	UZ-14 pore water (CHn)	28*	1.2	0.2	155	—	16	14	160	72.0	—	4	A
	UZ-14 perched water	25*	31	2.5	35	4.1	7.0	24.2	146.4	40.7	—	17.1	B
	WT-3 saturated zone	31.8	11.2	1.0	49.0	3.9	6.0	18.3	138.5	56.0	2.3	5.7	C
INEEL	Borehole W02 Lysimeter W0L01	5 to 10*	46.1	15	188	1.5	27	133	508	—	0.2	—	D
	Well 92 perched water (10/29/76)	13.5	29	17	120	12	81	64	290	22	0.4	—	E
	RWMC production well saturated zone	13	45	15	9.0	2.8	13	27	180.4	28	0.2	3.0	F

NOTE: \*estimated temperature

Sources: A = Yang et al. 1996 [100194], Table 3, sample UZ-14/1563.6-1563.8/up1,2,3.

B = Yang et al. 1996 [100194], Table 6, sample UZ-14D.

C = DTN: GS980908312322.008 [145412].

D = Dicke 1997 [157410], Table 5.

E = Rightmire and Lewis 1987 [156441], Table 13, sample of 10/29/1976.

F = USGS 2000 [157415], Table 4-2.



Table 10.3-2. Additional Water Inputs to the Waste-Disposal Area Due to Flooding

Year	Infiltration Rate (m/day)	Total Equivalent Depth of Infiltrating Water (m)
1962	$1.66 \times 10^{-2}$	0.166
1969	$1.24 \times 10^{-2}$	0.124
1982	$7.49 \times 10^{-3}$	0.075

Source: Magnuson and Sondrup 1998 [156431], Table 2-3.

Table 10.3-3. Hydrologic Properties Used in the One- and Two-Dimensional Single-Continuum and Dual-Permeability Models

Layer	Depth (m)	Porosity	Permeability (m <sup>2</sup> )	Residual Saturation, $S_{wr}$	Pore-size Distribution, $\lambda$	Air Entry Parameter, $\alpha$ (Pa <sup>-1</sup> )
Surficial sediments	0-5	0.50	$6.8 \times 10^{-13}$	0.194	0.401	$1.642 \times 10^{-4}$
Clay layer	5-6	0.05	$1.0 \times 10^{-15}$	0.246	0.273	$1.817 \times 10^{-4}$
A-basalt	6-9	0.01	$2.5 \times 10^{-12}$	0.010	0.500	$4.094 \times 10^{-4}$
AB (9 m) interbed	9-10	0.57	$1.0 \times 10^{-15}$	0.246	0.273	$1.817 \times 10^{-4}$
B-basalt	10-34	0.01	$2.5 \times 10^{-12}$	0.010	0.500	$4.094 \times 10^{-4}$
BC (34 m) interbed	34-36	0.48	$4.0 \times 10^{-15}$	0.083	0.273	$3.270 \times 10^{-4}$
C-basalt	36-73	0.01	$2.5 \times 10^{-12}$	0.010	0.500	$4.094 \times 10^{-4}$
CD (73 m) interbed	73-76	0.57	$4.0 \times 10^{-15}$	0.246	0.273	$1.817 \times 10^{-4}$
D-basalt	76-180	0.01	$2.5 \times 10^{-12}$	0.010	0.500	$4.094 \times 10^{-4}$
Basalt matrix		0.14	$5.0 \times 10^{-17}$	0.066	0.322	$3.917 \times 10^{-5}$

NOTE:  $\lambda$  and  $\alpha$  are pore-size distribution and air-entry parameters in the van Genuchten (1980 [100610]) moisture characteristic functions (see Lichtner 2001 [156429]).

Source: Simmons 2002 [157578], SN-LANL-SCI-234-V1, p. 22.

Table 10.3-4. Sorption Reaction Stoichiometry and Parameter Values for a Nonelectrostatic Description of Surface Complexation Reactions

Surface Complex Reaction						log K	z
Iron oxide							
$>\text{FeO}^-$	1 $>\text{FeOH}$	-1 $\text{H}^+$				8.930	-1
$>\text{FeOH}_2^+$	1 $>\text{FeOH}$	1 $\text{H}^+$				-7.290	1
$>\text{FeOAm}^{++}$	1 $>\text{FeOH}$	-1 $\text{H}^+$	1 $\text{Am}^{+++}$			-1.240	2
$>\text{FeOAm}(\text{OH})_2$	1 $>\text{FeOH}$	-3 $\text{H}^+$	1 $\text{Am}^{+++}$	2 $\text{H}_2\text{O}$		15.29	0
$>\text{FeOHPuO}_2^{++}$	1 $>\text{FeOH}$	1 $\text{H}^+$	1 $\text{PuO}_2^+$	-0.25 $\text{O}_2(\text{aq})$	-0.5 $\text{H}_2\text{O}$	-2.010	2
$>\text{FeOHPuO}_2$	1 $>\text{FeOH}$	-1 $\text{H}^+$	1 $\text{PuO}_2^+$	-0.25 $\text{O}_2(\text{aq})$	0.5 $\text{H}_2\text{O}$	6.210	0
$>\text{FeOHPuO}_2^+$	1 $>\text{FeOH}$	1 $\text{PuO}_2^+$				-4.790	1
$>\text{FeOHPuO}_3^-$	1 $>\text{FeOH}$	-2 $\text{H}^+$	1 $\text{PuO}_2^+$	1 $\text{H}_2\text{O}$		10.66	-1
$>\text{FeOHUO}_3$	1 $>\text{FeOH}$	-2 $\text{H}^+$	1 $\text{UO}_2^{++}$	1 $\text{H}_2\text{O}$		3.050	0
$>\text{FeOHUO}_2^{++}$	1 $>\text{FeOH}$	1 $\text{UO}_2^{++}$				-6.630	2
$>\text{FeOHNPuO}_2^+$	1 $>\text{FeOH}$	1 $\text{NpO}_2^+$				-4.320	1
$>\text{FeOHNPuO}_3^-$	1 $>\text{FeOH}$	-2 $\text{H}^+$	1 $\text{NpO}_2^+$	1 $\text{H}_2\text{O}$		11.26	-1
$>\text{FeOSr}^+$	1 $>\text{FeOH}$	-1 $\text{H}^+$	1 $\text{Sr}^{++}$			5.3	-1
$>\text{FeOSrOH}$	1 $>\text{FeOH}$	-2 $\text{H}^+$	1 $\text{Sr}^{++}$	1 $\text{H}_2\text{O}$		14.14	-1
Aluminosilicate							
$>\text{SiO}^-$	1 $>\text{SiOH}$	-1 $\text{H}^+$				7.200	-1
$>\text{SiOPuO}^+$	1 $>\text{SiOH}$	2 $\text{H}^+$	1 $\text{PuO}_2^+$	-0.25 $\text{O}_2(\text{aq})$	-0.5 $\text{H}_2\text{O}$	2.600	1
$>\text{SiOPuO}_2$	1 $>\text{SiOH}$	-1 $\text{H}^+$	1 $\text{PuO}_2^+$			6.430	0
$>\text{SiOPuO}_3\text{H}^-$	1 $>\text{SiOH}$	-2 $\text{H}^+$	1 $\text{PuO}_2^+$	1 $\text{H}_2\text{O}$		14.80	-1
$>\text{SiOUO}_3\text{H}$	1 $>\text{SiOH}$	-2 $\text{H}^+$	1 $\text{UO}_2^{++}$	1 $\text{H}_2\text{O}$		5.180	0
$>\text{SiOUO}_3^-$	1 $>\text{SiOH}$	-3 $\text{H}^+$	1 $\text{UO}_2^{++}$			12.35	-1
$>\text{SiONpO}_2$	1 $>\text{SiOH}$	-1 $\text{H}^+$	1 $\text{NpO}_2^+$			3.720	0
$>\text{SiONpO}_3\text{H}^-$	1 $>\text{SiOH}$	-2 $\text{H}^+$	1 $\text{NpO}_2^+$	1 $\text{H}_2\text{O}$		12.16	-1
$>\text{SiOAm}^{++}$	1 $>\text{SiOH}$	-1 $\text{H}^+$	1 $\text{Am}^{+++}$			-0.7	2
$>\text{SiOAmO}$	1 $>\text{SiOH}$	-3 $\text{H}^+$	1 $\text{Am}^{+++}$	1 $\text{H}_2\text{O}$		14.20	0
$>\text{AlO}^-$	1 $>\text{AlOH}$	-1 $\text{H}^+$				9.730	-1
$>\text{AlOH}^+$	1 $>\text{AlOH}$	1 $\text{H}^+$				-8.330	1
$>\text{AlOPuO}^+$	1 $>\text{AlOH}$	1 $\text{PuO}_2^+$	-0.25 $\text{O}_2(\text{aq})$	-0.5 $\text{H}_2\text{O}$		-1.03	1
$>\text{AlOPuO}_2^-$	1 $>\text{AlOH}$	-2 $\text{H}^+$	1 $\text{PuO}_2^+$	-0.25 $\text{O}_2(\text{aq})$	0.5 $\text{H}_2\text{O}$	16.85	-1
$>\text{AlOPuO}_2$	1 $>\text{AlOH}$	1 $\text{PuO}_2^+$				3.090	0
$>\text{AlOUO}_2^+$	1 $>\text{AlOH}$	-1 $\text{H}^+$	1 $\text{UO}_2^{++}$			-3.130	1
$>\text{AlONpO}_2$	1 $>\text{AlOH}$	-1 $\text{H}^+$	1 $\text{NpO}_2^+$			4.670	0
$>\text{AlONpO}_3\text{H}^-$	1 $>\text{AlOH}$	-2 $\text{H}^+$	1 $\text{NpO}_2^+$	1 $\text{H}_2\text{O}$		14.26	-1
$>\text{AlOAm}^{++}$	1 $>\text{AlOH}$	-1 $\text{H}^+$	1 $\text{Am}^{+++}$			-2.490	2
Calcite							
$>\text{PuO}_2^+$	1 $>\text{Ca}^{++}$	-1 $\text{Ca}^{++}$	1 $\text{PuO}_2^+$			-1.850	1
$>\text{UO}_2^{++}$	1 $>\text{Ca}^{++}$	-1 $\text{Ca}^{++}$	1 $\text{UO}_2^{++}$			-5.120	2
$>\text{NpO}_2^+$	1 $>\text{Ca}^{++}$	-1 $\text{Ca}^{++}$	1 $\text{NpO}_2^+$			-2.350	1
$>\text{AmCO}_3^+$	1 $>\text{Ca}^{++}$	-1 $\text{Ca}^{++}$	1 $\text{HCO}_3^-$	-1 $\text{H}^+$	1 $\text{Am}^{+++}$	-1.587	1
$>\text{Sr}^{++}$	1 $>\text{Ca}^{++}$	-1 $\text{Ca}^{++}$	1 $\text{Sr}^{++}$			1.750	1

Source: Simmons 2002 [157578], SN-LANL-SCI-234-VI, p.29.

Table 10.3-5. Ion Exchange Selectivity Coefficients and Fitted Cation Exchange Capacity (CEC)

Cation	Selectivity Coefficient
Na <sup>+</sup>	1.
Cs <sup>+</sup>	12.5
Sr <sup>++</sup>	2.857
K <sup>+</sup>	5.
Mg <sup>++</sup>	2.
Ca <sup>++</sup>	2.5
	<b>CEC (mol/kg solid)</b>
	0.02

NOTE: Selectivity coefficients modified from Appelo 1996 [156425], pp. 197.

Source: Simmons 2002 [157578], SN-LANL-SCI-234-V1, p. 28.

Table 10.3-6. Composition of Injected Fluid

Table 10.3-6a. Primary Species Properties					
Species	Molality	Total Concentration	Activity Coeff.	Species Activity Ratio/H <sup>+</sup>	Constraint
Ca <sup>++</sup>	6.7143 x 10 <sup>-4</sup>	7.2355 x 10 <sup>-4</sup>	6.7444 x 10 <sup>-1</sup>	1.1936 x 10 <sup>1</sup>	1 total
K <sup>+</sup>	3.0692 x 10 <sup>-4</sup>	3.0692 x 10 <sup>-4</sup>	8.9884 x 10 <sup>-1</sup>	4.0415	1 total
Mg <sup>++</sup>	6.3025 x 10 <sup>-4</sup>	6.9944 x 10 <sup>-4</sup>	6.8849 x 10 <sup>-1</sup>	1.1908 x 10 <sup>1</sup>	1 total
Na <sup>+</sup>	5.2197 x 10 <sup>-3</sup>	5.2197 x 10 <sup>-3</sup>	9.0166 x 10 <sup>-1</sup>	5.2721	1 total
Cl <sup>-</sup>	2.4696 x 10 <sup>-3</sup>	2.4706 x 10 <sup>-3</sup>	8.9884 x 10 <sup>-1</sup>	-1.0162 x 10 <sup>1</sup>	-1 charge
SO <sub>4</sub> <sup>-2</sup>	5.9941 x 10 <sup>-4</sup>	6.6627 x 10 <sup>-4</sup>	6.5908 x 10 <sup>-1</sup>	-1.8331 x 10 <sup>1</sup>	1 total
HCO <sub>3</sub> <sup>-</sup>	4.4631 x 10 <sup>-3</sup>	4.7528 x 10 <sup>-3</sup>	9.0166 x 10 <sup>-1</sup>	-9.9048	1 total
F <sup>-</sup>	1.9919 x 10 <sup>-5</sup>	2.0154 x 10 <sup>-5</sup>	9.0027 x 10 <sup>-1</sup>	-1.2255 x 10 <sup>1</sup>	1 total
SiO <sub>2</sub> (aq)	3.6615 x 10 <sup>-4</sup>	3.6615 x 10 <sup>-4</sup>	1.0000	-3.4363	1 total
H <sup>+</sup>	2.7897 x 10 <sup>-8</sup>	2.0345 x 10 <sup>-4</sup>	9.1373 x 10 <sup>-1</sup>	0.0000	3 calcite
Al <sup>+++</sup>	3.5938 x 10 <sup>-17</sup>	5.5068 x 10 <sup>-10</sup>	4.4062 x 10 <sup>-1</sup>	6.2189	3 K-feldspar
Fe <sup>++</sup>	1.0078 x 10 <sup>-11</sup>	1.6446 x 10 <sup>-11</sup>	6.7444 x 10 <sup>-1</sup>	4.1123	3 goethite
Sr <sup>++</sup>	4.7300 x 10 <sup>-13</sup>	5.0000 x 10 <sup>-13</sup>	6.6693 x 10 <sup>-1</sup>	2.7837	1 total
PuO <sub>2</sub> <sup>+</sup>	9.9671 x 10 <sup>-15</sup>	4.0000 x 10 <sup>-9</sup>	9.0166 x 10 <sup>-1</sup>	-6.4470	1 total
UO <sub>2</sub> <sup>++</sup>	1.1940 x 10 <sup>-17</sup>	1.1110 x 10 <sup>-10</sup>	6.6305 x 10 <sup>-1</sup>	-1.8141	1 total
NpO <sub>2</sub> <sup>+</sup>	7.1760 x 10 <sup>-11</sup>	1.1150 x 10 <sup>-10</sup>	9.0166 x 10 <sup>-1</sup>	-2.5897	1 total
Am <sup>+++</sup>	7.5783 x 10 <sup>-14</sup>	2.0000 x 10 <sup>-11</sup>	4.0148 x 10 <sup>-1</sup>	9.5429	1 total
Cs <sup>+</sup>	4.0000 x 10 <sup>-13</sup>	4.0000 x 10 <sup>-13</sup>	8.9736 x 10 <sup>-1</sup>	-4.8435	1 total
O <sub>2</sub> (aq)	1.2611 x 10 <sup>-48</sup>	-1.0030 x 10 <sup>-9</sup>	1.0000	-4.7899 x 10 <sup>1</sup>	4 O <sub>2</sub> (g)
Solution conditions:					
Temperature: 25.0°C		Ionic strength: 1.0087 x 10 <sup>-2</sup>		Solution density: 0.99780 g/cm <sup>3</sup>	
pH: 7.5936		pe: 1.931		Eh: 1.1430 x 10 <sup>-1</sup> V	
Charge balance: -q = -6.3071 x 10 <sup>-16</sup>					
Computational parameters:					
Boundary condition: type 1			Iterations: 5		

Source: Simmons 2002 [157578], SN-LANL-SCI-234-V1, p. 31.

Table 10.3-6 continued. Composition of Injected Fluid

Table 10.3-6b. Properties of Complexes				
Complex	Molality	Activity Coeff.	Species Activity/H <sup>+</sup>	log K
CO <sub>2</sub> (aq)	2.25165 x 10 <sup>-4</sup>	1.0000	-3.6475	6.3414
MgSO <sub>4</sub> (aq)	4.43159 x 10 <sup>-5</sup>	1.0000	-4.3534	2.4125
CaSO <sub>4</sub> (aq)	2.25424 x 10 <sup>-5</sup>	1.0000	-4.6470	2.1004
CaHCO <sub>3</sub> <sup>+</sup>	2.23075 x 10 <sup>-5</sup>	0.90166	2.9029	1.0429
MgHCO <sub>3</sub> <sup>+</sup>	2.08899 x 10 <sup>-5</sup>	0.90166	2.8744	1.0329
CO <sub>3</sub> <sup>-2</sup>	1.12691 x 10 <sup>-5</sup>	0.66305	-20.057	-10.325
CaCO <sub>3</sub> (aq)	7.00620 x 10 <sup>-6</sup>	1.0000	-5.1545	-7.0088
MgCO <sub>3</sub> (aq)	3.01655 x 10 <sup>-6</sup>	1.0000	-5.5205	-7.3562
MgCl <sup>+</sup>	7.76285 x 10 <sup>-7</sup>	0.90166	1.4445	-0.13865
OH <sup>-</sup>	4.44777 x 10 <sup>-7</sup>	0.90027	-13.906	-13.991
CaCl <sup>+</sup>	2.22229 x 10 <sup>-7</sup>	0.90166	0.90124	-0.70039
MgF <sup>+</sup>	1.92570 x 10 <sup>-7</sup>	0.90166	0.83903	1.3486
CaF <sup>+</sup>	4.28435 x 10 <sup>-8</sup>	0.90166	0.18632	0.67736
Pu(OH) <sub>4</sub> (aq)	3.99990 x 10 <sup>-9</sup>	1.0000	-8.3980	-13.920
CaOH <sup>+</sup>	2.78300 x 10 <sup>-9</sup>	0.90166	-1.0010	-12.850
AlO <sub>2</sub> <sup>-</sup>	5.49982 x 10 <sup>-10</sup>	0.90166	-16.814	-22.879
CaCl <sub>2</sub> (aq)	4.95545 x 10 <sup>-10</sup>	1.0000	-9.3049	-0.65346
UO <sub>2</sub> (CO <sub>3</sub> ) <sub>3</sub> <sup>-4</sup>	5.83351 x 10 <sup>-11</sup>	0.18815	-40.452	-9.4530
UO <sub>2</sub> (CO <sub>3</sub> ) <sub>2</sub> <sup>-2</sup>	5.18682 x 10 <sup>-11</sup>	0.65908	-25.394	-3.7613

Source: Simmons 2002 [157578], SN-LANL-SCI-234-V1, p. 90.

**Table 10.3-6c. Mineral Saturation Indices**

Mineral	Saturation Index	log K
Dolomite	1.16594	-2.52402
Hematite	$9.59704 \times 10^{-1}$	$1.68702 \times 10^1$
Quartz	$5.69305 \times 10^{-1}$	4.00565
Chalcedony	$2.98104 \times 10^{-1}$	3.73444
Goethite	0.00000	7.95526
Calcite	0.00000	-1.85424
K-feldspar	0.00000	$2.94216 \times 10^{-1}$
$\text{Pu}(\text{OH})_4$	$-1.57462 \times 10^{-1}$	-5.67951
Magnesite	$-4.62767 \times 10^{-1}$	-2.29848
$\text{SiO}_2(\text{am})$	$-7.16385 \times 10^{-1}$	2.71996
Kaolinite	-1.70898	-6.79726
Gibbsite	-1.77543	-7.75591
Muscovite	-1.90002	$-1.35668 \times 10^1$
Gypsum	-2.27448	4.47292
Beidellite-Ca	-2.29087	-5.56815
Sepiolite	-3.72692	$-3.04075 \times 10^1$
Brucite	-4.47379	$-1.62984 \times 10^1$
Magnetite	-5.38525	6.50570

Source: Simmons 2002 [157578], SN-LANL-SCI-234-V1, p. 32.

**Table 10.3-6d. Gas Compositions**

Gas	log Partial Pressure	Pressure (bars)	log K
$\text{O}_2(\text{g})$	-45.00	$1.0000 \times 10^{-45}$	2.8993
$\text{CO}_2(\text{g})$	-2.180	$6.6104 \times 10^{-3}$	7.8092

Source: Simmons 2002 [157578], SN-LANL-SCI-234-V1, p. 32.

Table 10.3-7. Fitted Surface Complexation Site Densities

Site	Concentration (mol/bulk dm <sup>3</sup> )
>FeOH	$4.0 \times 10^{-7}$
>AlOH, >SiOH	$5.0 \times 10^{-6}$
>Ca <sup>++</sup>	$1.0 \times 10^{-7}$

Source: Simmons 2002 [157578], SN-LANL-SCI-234-V1, p. 28.

Table 10.3-8. Contribution of Radionuclides to Surface Complexation Sites

Component	Site	Mineral $K_d$ (dm <sup>3</sup> /dm <sup>3</sup> )	Retardation: $1 + K_d$	% Adsorbed
Sr <sup>++</sup>	>FeOH	$5.9996 \times 10^{-5}$		
	>SiOH	0.0000		
	>AlOH	0.0000		
	>Ca <sup>++</sup>	$4.9530 \times 10^{-6}$		
Total of all sites:		$6.4949 \times 10^{-5}$	1.0001	$6.4945 \times 10^{-3}$
PuO <sub>2</sub> <sup>+</sup>	>FeOH	$2.3473 \times 10^1$		
	>SiOH	$1.7024 \times 10^{-11}$		
	>AlOH	$3.4754 \times 10^1$		
	>Ca <sup>++</sup>	$7.0217 \times 10^{-8}$		
Total of all sites:		$5.8227 \times 10^1$	$5.9227 \times 10^1$	$9.8312 \times 10^1$
UO <sub>2</sub> <sup>++</sup>	>FeOH	$4.4734 \times 10^{-2}$		
	>SiOH	$1.1785 \times 10^{-3}$		
	>AlOH	$5.7571 \times 10^{-3}$		
	>Ca <sup>++</sup>	$4.1468 \times 10^{-6}$		
Total of all sites:		$5.1674 \times 10^{-2}$	1.0517	4.9135
NpO <sub>2</sub> <sup>+</sup>	>FeOH	$7.7954 \times 10^{-3}$		
	>SiOH	$7.5785 \times 10^4$		
	>AlOH	$7.5055 \times 10^{-4}$		
	>Ca <sup>++</sup>	$5.7351 \times 10^{-2}$		
Total of all sites:		$7.5785 \times 10^4$	$7.5786 \times 10^4$	$9.9999 \times 10^1$
Am <sup>+++</sup>	>FeOH	$4.9624 \times 10^{-1}$		
	>SiOH	$3.9129 \times 10^{-1}$		
	>AlOH	$2.8157 \times 10^1$		
	>Ca <sup>++</sup>	4.0926		
Total of all sites:		$3.3137 \times 10^1$	$3.4137 \times 10^1$	$9.7071 \times 10^1$

Source: Simmons 2002 [157578], SN-LANL-SCI-234-V1, p. 33.

Table 10.4-1. Measurements of U-Th Isotopic Composition and Concentration in Various Water Samples Collected near the Nopal I Uranium Deposit

Sampling Location	Sample ID	Collection Date	U (ppb)	(+/-) (%)	$^{234}\text{U}/^{238}\text{U}$ atom ratio ( $\times 10^{-6}$ )	(+/-) (%)	$\delta\text{D}$ (‰)	$\delta^{18}\text{O}$ (‰)	Notes
Perched water from borehole at +10 level	BH12W95-5	August 1995	4.79	0.20	119.66	0.18			
	BH12W95-11	September 1995	5.77	0.25	120.86	0.14			
	AS-5	25 February 2000	5.73	0.19	156.75	0.10	-64	-9.3	
8.5 m into north part of adit at +00 level	030701-2001	7 March 2001	10.40	0.19	112.59	0.11			
	ADIT95-6	September 1995	0.20	2.4	278.40	0.16			
	AS-4	25 February 2000	2.87	0.30	121.15	0.25	-1	-2.8	
23 m from adit entrance	030701-02	7 March 2001	1.20	0.24	142.05	0.20			E in Figure 10.4-1
	ADIT95-9	September 1995	0.89	0.54	156.16	0.11			
	AS-3	February 2000	4.03	0.19	64.61	0.18	-7	-3.6	
15 m from adit entrance	030701-03	7 March 2001	26.96	0.18	64.36	0.10			D in Figure 10.4-1
	AS-2	25 February 2000	36.92	0.19	51.53	0.16	-7	-3.4	
	030701-04	7 March 2001	16.49	0.28	50.51	0.40			C in Figures 10.4-1, 10.4-2
12 m from adit entrance	AS-1	25 February 2000	68.46	0.19	58.21	0.14	-11	-2.5	B in Figures 10.4-1, 10.4-2
5 m from adit entrance	030701-05	7 March 2001	13.01	0.23	56.14	0.20			A in Figures 10.4-1, 10.4-2
Abandoned mining camp supply well	AS-6	25 February 2000	2.53	0.25	64.93	0.30			
Poços Ranch	WVW95-03	September 1995	0.17	2.8	76.02	0.22			Well
	AS-7	25 February 2000	0.27	1.0	140.00	1.0	-61	-8.7	Holding Tank
	030701-06	7 March 2001	5.71	0.19	111.69	0.10			Holding Tank

Source: 1995 samples from Pickett and Murphy 1999 [110009], Table II.  
2000 and 2001 samples from Simmons 2002 [157578], SN-LANL-SCI-108-V1, p. 16; SN-LBNL-SCI-108-V1, pp. 86, 87.



## 11. ANALOGUES TO THERMALLY COUPLED PROCESSES

### 11.1 INTRODUCTION

Numerous igneous-intrusion contact zones have been examined with the objective of understanding chemical reactions and migration of elements away from the heated contact zone, as well as understanding thermal-hydrologic-chemical (THC) effects. A number of these studies are described in CRWMS M&O (2000 [141407]; 2000 [151945], Section 13), as summarized by the following.

The effects of shallow (<500 m) magmatic intrusions into unsaturated host rocks can be quite different from effects associated with deeper hydrothermal systems. Deeper, saturated hydrothermal systems may display evidence that a large-scale hydrothermal cell was established (Brookins 1986 [109877], p. 337). In contrast, both the Banco Bonito study (Stockman et al. 1994 [117820], p. 88) and the Grants Ridge basalt intrusion study (WoldeGabriel et al. 1999 [110071], p. 409) indicate that the effects of high-temperature (~850°C; Stockman et al. 1994 [117820], p. 88) intrusions into these unsaturated environments appear to have been slight, to have been limited to within 10 m or so of the contacts, and to show no evidence of fluid-driven convective heat transfer or pervasive hydrothermal alteration of the country rock. These field studies, along with the Paiute Ridge field studies (see Section 11.4), provide limiting high-temperature-case natural analogues for evaluating THC processes resulting from the heat released by the decay of radioactive waste in an unsaturated environment.

A good analogy for understanding future water-rock interactions at the mountain scale is the fossil hydrothermal system at Yucca Mountain itself. Most zeolitic alteration occurred 13 to 11.6 Ma, at about the same time as tuff emplacement (Bish and Aronson 1993 [100006], p. 148). After formation of the major zeolitic horizons, deep-seated hydrothermal activity persisted until about 10 Ma. This activity was evidently limited to temperatures of 90–100°C, because at prolonged exposure to temperatures greater than 90°C, the sorptive zeolites clinoptilolite and mordenite are altered to the nonsorptive minerals analcime plus quartz and/or calcite, and this transformation did not occur.

Section 11 reports analyses conducted since CRWMS M&O 2000 [141407] of THC and thermal-hydrologic-mechanical (THM) natural analogue studies. Section 11.2 presents the results of an extensive survey of geothermal literature for the purpose of obtaining insights from coupled processes operating in geothermal fields. Section 11.3 then provides a detailed examination of THC processes relevant to the Yucca Mountain drift-scale system, observed at the Yellowstone, Wyoming, geothermal field. Section 11.4 presents results of a field investigation and modeling study of evidence left in a fossil hydrothermal system at Paiute Ridge, Nevada. Next, examples are given in Section 11.5 of evidence for THC effects on transport. Section 11.6 reports THM effects to a potential repository from a number of settings with analogous conditions. Finally, Section 11.7 summarizes what can be learned about THC and THM coupled processes relevant to a potential high-level waste repository at Yucca Mountain. Information found in Sections 11.2 through 11.5 may help to support arguments associated with KTI KUZ 0407 listed in Table 1-1.

## **11.2 GEOTHERMAL ANALOGUES TO YUCCA MOUNTAIN THERMAL-HYDROLOGIC-CHEMICAL PROCESSES**

### **11.2.1 Objectives**

The goal of Section 11.2 is to demonstrate the utility of geothermal systems as natural analogues for processes that are expected to occur in the potential Yucca Mountain repository. The primary objective of Section 11.2 is to use geothermal systems as natural analogues for illustrating coupled processes that impact permeability, fluid flow, and chemical transport. The introduction to this section notes some of the key THC processes observed in geothermal systems, and how these processes might impact the potential Yucca Mountain repository. A summary of key components of geothermal systems is then presented, followed by a description of the potential Yucca Mountain repository and a discussion of limitations of geothermal analogues for the Yucca Mountain system. The main body of this report consists of descriptions of geothermal analogues for each of the key THC processes identified. This is followed by a discussion of how these processes could impact the total site performance. Finally, suggestions are made for additional work that would further extend the use of geothermal systems in the validation and confirmation of Yucca Mountain models. The initial stages of a literature survey identified the Yellowstone geothermal system as particularly relevant for the Yucca Mountain system. Detailed analysis of core samples from Yellowstone was conducted to supplement previous studies of the Yellowstone geothermal system. The results of this work are described in detail in Section 11.3 of this report.

### **11.2.2 Introduction**

Geothermal systems can be used as a natural laboratory for examining many of the coupled THC processes expected for the potential nuclear waste repository at Yucca Mountain, Nevada (Simmons and Bodvarsson 1997 [126511]; CRWMS M&O 2000 [141407]). Key processes that are expected to occur in the potential high-level nuclear waste repository at Yucca Mountain, such as boiling and condensation and mineral dissolution and precipitation, and their effects on permeability, fluid flow, and radionuclide transport, can be observed in many geothermal systems. Prior use of geothermal systems as natural analogues has focused on the verification of geochemical models (e.g., Meijer 1987 [101345]; Apps 1995 [154615]; Bruton et al. 1995 [117033]). However, active and fossil geothermal systems can also yield important insights into the consequences of processes such as boiling, condensation, fluid mixing, and water-rock interaction associated with fluid flow in matrix and fractures (Figure 11.2-1). These systems allow observation of the effects of processes over much longer time scales than are possible in laboratory or field testing, and provide a benchmark for coupled process modeling. Characterization of the effects of water-rock interaction (such as mineral precipitation and dissolution) on matrix and fracture permeability in geothermal systems can then be used to estimate potential changes in fluid flow resulting from the thermal impact of storing high-level nuclear wastes in fractured ash flow tuffs.

This study builds upon an earlier review of geothermal systems as natural analogues (Simmons and Bodvarsson 1997 [126511]; CRWMS M&O 2000 [141407]). This study expands the scope of the earlier review by including additional THC processes that are observed in geothermal systems and incorporates the results of new geothermal studies as part of a literature review.